Magnetic Field Sensing and

Nanoparticle Induced Ferromagnetism in Graphene Towards Spintronics

by

Guibin Song

A Dissertation Presented in Partial Fulfillment
of the Requirements for the Degree
Doctor of Philosophy

Approved April 2019 by the
Graduate Supervisory Committee:

Richard A. Kiehl, Chair
Hongbin Yu
Tingyong Chen
Nicholas D. Rizzo

ARIZONA STATE UNIVERSITY

August 2019

ABSTRACT

Graphene has been extensively researched for both scientific and technological interests since its first isolation from graphite. The excellent transport properties and long spin diffusion length of graphene make it a promising material for electronic and spintronic device applications. This dissertation deals with the optimization of magnetic field sensing in graphene and the realization of nanoparticle induced ferromagnetism in graphene towards spintronic device applications.

Graphene has been used as a channel material for magnetic sensors demonstrating the potential for very high sensitivities, especially for Hall sensors, due to its extremely high mobility and low carrier concentration. However, the two-carrier nature of graphene near the charge neutrality point (CNP) causes a nonlinearity issue for graphene Hall sensors, which limits useful operating ranges and has not been fully studied. In this dissertation, a two-channel model was used to describe the transport of graphene near the CNP. The model was carefully validated by experiments and then was used to explore the optimization of graphene sensor performance by tuning the gate operating bias under realistic constraints on linearity and power dissipation.

The manipulation of spin in graphene that is desired for spintronic applications is limited by its weak spin-orbit coupling (SOC). Proximity induced ferromagnetism (PIFM) from an adjacent ferromagnetic insulator (FMI) provides a method for enhancing SOC in graphene without degrading its transport properties. However, suitable FMIs are uncommon and difficult to integrate with graphene. In this dissertation, PIFM in graphene from an adjacent Fe_3O_4 magnetic nanoparticle (MNP) array was demonstrated

for the first time. Observation of the anomalous Hall effect (AHE) in the device structures provided the signature of PIFM. Comparison of the test samples with different control samples conclusively proved that exchange interaction at the MNP/graphene interface was responsible for the observed characteristics. The PIFM in graphene was shown to persist at room temperature and to be gate-tunable, which are desirable features for electrically controlled spintronic device applications.

The observation of PIFM in the MNP/graphene devices indicates that the spin transfer torque (STT) from spin-polarized current in the graphene can interact with the magnetization of the MNPs. If there is sufficient STT, spin torque oscillation (STO) could be realized in this structure. In this dissertation, three methods were employed to search for signatures of STO in the devices. STO was not observed in our devices, most likely due to the weak spin-polarization for current injected from conventional ferromagnetic contacts to graphene. Calculation indicates that graphene should provide sufficient spin-polarized current for exciting STO in optimized structures that miniaturize the device area and utilize optimized tunnel-barrier contacts for improved spin injection.

DEDICATION

To my parents.

ACKNOWLEDGEMENTS

I would first like to thank my supervisor, Prof. Richard A. Kiehl, for offering me the opportunity to do research in this group. This dissertation would not have been possible without his continuous support of my graduate study and research. Prof. Kiehl has been patiently guiding me and encouraging me in the research and experiment. He helped me a lot in learning fundamentals, developing my ideas and solving technical problems. He also spent a great amount of time on helping me in writing papers and preparing presentations. I have learned so much from him not only about research but also about career and life.

I would also like to thank my committee members, Prof. Hongbin Yu, Prof. Tingyong Chen and Dr. Nicholas D. Rizzo, for their constructive discussions and suggestions during my presentations and afterwards. Their insightful comments helped the development of this work. I would like to thank to Dr. Rizzo for his help in my learning about magnetism and related measurements and analysis.

I would like to thank my colleague, Dr. Mojtaba Ranjbar, for helping me set up the equipment in our lab, teaching me about measurement tools and helping me on the experiments. His expertise has always been helpful on my research. I have also benefited a lot from his encouragement and advice on my career.

I would like to thank Prof. Nathan Newman for providing me access to his VSM system and I would also like to thank his student Kaiwen Zheng for helping me in the measurements. I would like to thank Prof. David J. Smith and Prof. Martha R.

McCartney for their help in the TEM imaging for my sample. I would like to thank Dr. Mark W. Keller at NIST for preparing me graphene samples.

I would like to thank Dr. Gejian Zhao and Dr. Runchen Fang for their help when I set up the lab. I would like to thank Zhiyu Huang for his help in preliminary analysis of some experimental data.

I would like to express my sincere gratitude to staffs at ASU NanoFab, Dr. Stefan Myhajlenko, Carrie Sinclair, Kevin Nordquist, Todd Eller, Kevin Hilgers and Arthur Handugan, for training me on fabrication and characterization tools and for helping me responsively and supportively. I would also like to thank staffs in Eyring Materials Center at ASU, Dr. Emmanuel Soignard and David Wright, for training me on characterization and processing tools. I would like to thank Hamdi Mani for his help on RF equipment and wire bonding.

I would like to thank my parents and other family members for their love and support. I would like to thank Dr. Jing Gao, for all her love and support during the difficult time in my graduate study and in writing of this dissertation.

Finally, I would like to thank all colleagues and all my friends for their support in my work and my life.

TABLE OF CONTENTS

Page

CHAPTER Page

CHAPTER Page

Page

LIST OF TABLES

Table Page

LIST OF FIGURES

Figure Page

CHAPTER 1

INTRODUCTION

Since its isolation from graphite by exfoliation, graphene attracts much interest because of its excellent properties, especially the extremely high carrier mobility and long spin life time for electronic and spintronic applications [1–6]. Graphene has a unique Dirac-cone band structure without a band gap and the carrier type can be changed to electron or hole by applying a gate bias. Back gated graphene devices, such as field-effect transistors (FETs) and Hall bars, have been widely adopted for scientific research and possible applications due to their simplicity for obtaining gate tunability. Chemical vapor deposition (CVD) of graphene and transfer technique for graphene onto different substrates make it possible for batch-fabrication of graphene devices in a large scale [7–10].

Graphene has been studied as a channel material for magnetic field sensors, including both magnetoresistance [11–13] and Hall sensors [14–17], and has shown promise for realizing extraordinarily high sensitivities due to its high mobility and unique electrical properties. In particular, graphene Hall sensors show much higher sensitivities than conventional semiconductor Hall sensors [16,18]. However, a nonlinearity issue for graphene Hall sensors due to its two-carrier nature, which limits useful operating ranges, has not been well studied. The optimization of operating gate bias is essential to balance the trade-off between high sensitivity and good linearity of a graphene Hall sensor. A two-channel model was used here to analyze the linearity issue and to optimize the graphene Hall sensor operation.

Spin injection from ferromagnetic contacts and spin transport in graphene have been studied in the past decade [19–23]. Making graphene ferromagnetic is challenging but attracts much attention from both scientific and technological points of view [24]. Magnetic moments in graphene due to vacancy defects and adatoms have been studied [2,24,25]. However, scattering caused by these random impurities could greatly reduce the excellent electrical properties of graphene, i.e. the high mobility. Recently, Proximity induced ferromagnetism (PIFM) in graphene from a ferromagnetic insulator (FMI) thin film has been achieved in several systems without dramatically degrading graphene's excellent transport properties; examples are graphene on yttrium iron garnet (YIG) [26,27] and EuS [28,29] systems. However, FMIs are limited in number and are difficult to fabricate and integrate with graphene, which greatly limits the possibilities for practical applications. Here, an alternative method is introduced to achieve PIFM in graphene from isolated magnetic nanoparticles (MNPs), instead of FMI thin films. The PIFM in graphene from MNPs was demonstrated for the first time in the experiments. This greatly expands the range of ferromagnetic materials from insulators to conductive semiconductors, semimetals and metals, and it provides a simple and low-cost way to achieve PIFM in graphene for a large scale and opens possibilities for novel spintronic devices.

Spin-transfer torque (STT) is a new mechanism for producing microwave oscillations based on the precession of magnetization and the magnetoresistance effect [30]. STT from a spin polarized current is the key to keep a sustained precession by balancing the damping torque. Spin torque nano-oscillators (STNOs) using giant magnetoresistance (GMR) and tunneling magnetoresistance (TMR) have been widely

studied in previous research [31–35]. However, it is difficult to achieve phase locking of GMR or TMR based STNOs in an array due to the challenging in fabrication for STNO with small size down to 10's of nm and the large device-to-device variations for structures patterned at lithographic limits. Phase locking of an array of STNOs can potentially increase the output power and improve the spectral purity [35]. The use of monodisperse ferromagnetic nanoparticles laid out in a highly uniform self-assembled array, offers a promising scheme for realizing STNO in a large array with a simple fabrication process. The PIFM in graphene demonstrated in these experiments provides a signature for STT excitation of the MNPs, which is essential for spin torque oscillation (STO).

Following the introduction in this chapter, the dissertation is organized as below.

In Chapter 2, I focus on the device fabrication process and characterizations. First, I describe the device fabrication for this dissertation using photolithography and then I present the basic device characterization results. Next, I explain the self-assembly technique used to form the Fe_3O_4 MNPs arrays, followed by the shell removal technique and the magnetization characterization of MNP arrays. I also introduce Hall measurement and STO measurement methods.

In Chapter 3, I describe the two-channel model used to study the magnetoresistance characteristics and nonlinear Hall characteristics of graphene related to its two-carrier nature near the Dirac point. The two-channel model is validated by experiments and used for the discussions on linearity and realizable sensitivities of graphene Hall sensors. Next, I explored the operation of graphene magnetic sensors and

predicted the sensitivities of graphene Hall sensors under linearity and power constraints using the two-channel model.

In Chapter 4, I present the Hall measurement results for both control and test devices. I demonstrate PIFM in graphene from MNPs using anomalous Hall effect (AHE) using well-designed control experiments to conclusively prove the exchange interaction at the MNP/graphene interface. Results on the temperature dependence and gate tunability of PIFM in graphene are presented

In Chapter 5, I introduce STNO and explore the possibility of realizing STO using the MNP/graphene structure. Measurement methods for detecting STT and spin torque oscillation are explained, and preliminary results are presented. I then discuss the current issues and future plans for improving the devices and measurements.

In Chapter 6, an overall summary of the dissertation is given.

CHAPTER 2

DEVICE FABRICATION AND CHARACTERIZATION

In this chapter, I describe the process of device fabrication for preparing back-gated graphene FETs and Hall bars using photolithography. I then present the basic device characterization results, including *I-V* characteristics and Raman spectrum. Next, I explain the self-assembly technique to form Fe_3O_4 MNP array. The MNP array was imaged by scanning electron microscope (SEM) and transmission electron microscopy (TEM). The annealing method to remove the organic shell of MNPs was tested and successful removal of the shell was confirmed by Fourier-transform infrared spectroscopy (FTIR) and conductive atomic force microscope (C-AFM). Magnetization characterization of the MNP array was studied by vibrating-sample magnetometer (VSM). I also introduce the Hall measurement and STO measurement system for later experiments.

2.1 Back-gated graphene device fabrication

Back-gated six-arm Hall bar structures and FETs were fabricated for these experiments using commercially available graphene that is deposited by CVD and transferred to a SiO_2 (285 nm)/p-Si substrate. The device fabrication flow is shown in Figure 2.1. First, the substrate was cleaned by acetone and rinsed by isopropyl alcohol (IPA). Photolithography followed by plasma dry etching was used to pattern the graphene channel region. The photoresist used here is AZ3312 and the spin coating is 3500 rpm which gives a 1-μm photoresist (PR). The uncovered graphene was etched

away in 100 W oxygen plasma for 2 minutes. The PR was then removed by acetone. Next, a standard photoresist lift-off process was performed to form metal contacts comprised of Ti/Au (10/120 nm) layers deposited by electron beam evaporation. PR used in the second lithography is AZ4330 and the spin coating is 3500 rpm, which gives a 3-μm PR. The lift-off process was performed in acetone with ultrasonic assistance. MNPs can be deposited later on the surface of the fabricated device using drop-casting or liquid-air self-assembly technique to form MNP/graphene device structure, which will be addressed in the following sections.

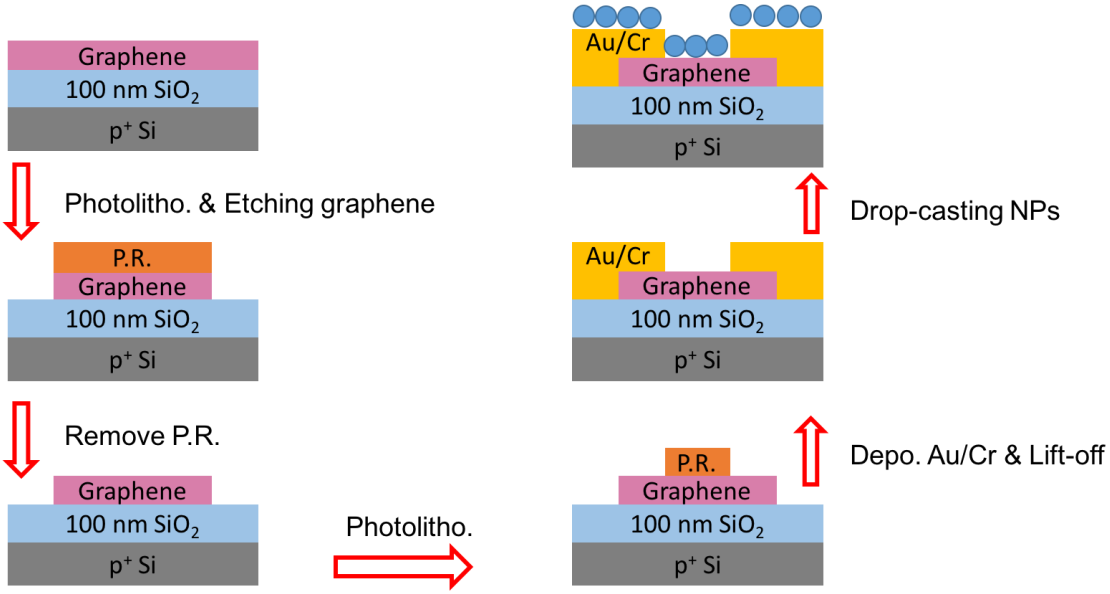

Figure 2.1 Fabrication flow of back-gated graphene devices. Typical photolithography and lift-off technique are used to define the graphene channel and to make contacts. MNPs can be deposited on the fabricated device using drop-casting technique.

2.2 Device quality characterizations

A schematic structure of the Hall bar device is shown in Figure 2.2a. The drain current I_d vs gate bias V_g characteristic at fixed drain bias V_d = 0.1 V is shown in Figure 2.2b for a Hall bar device with channel width and length of 30 μm and 60 μm, respectively. The I_d shows a minimum at V_g close to 0 V, which is the charge neutrality point (CNP). The symmetry of the I_d-V_g curve around CNP indicates a good electrical contact has been obtained in the graphene channel for both electron and hole bias regimes.

Raman spectroscopy was used to determine the quality and the number of layers of the graphene channel. The prominent modes in Figure 2.3c are associated with the G mode at 1584 cm^{-1} and 2D the mode at 2685 cm^{-1}. Fitting the 2D peak by a single Lorentzian distribution gives a full-width at half-maximum (FWHM) of 43 cm^{-1}, as shown in Figure 2.2d. The peak position, width of the peaks and single Lorentzian fitting of the 2D peak indicate that the channel consists monolayer graphene [36–38]. The weak peak D at 1346 cm^{-1} in Figure 2.2c indicates that a moderate level of defects exists in the channel [37,39].

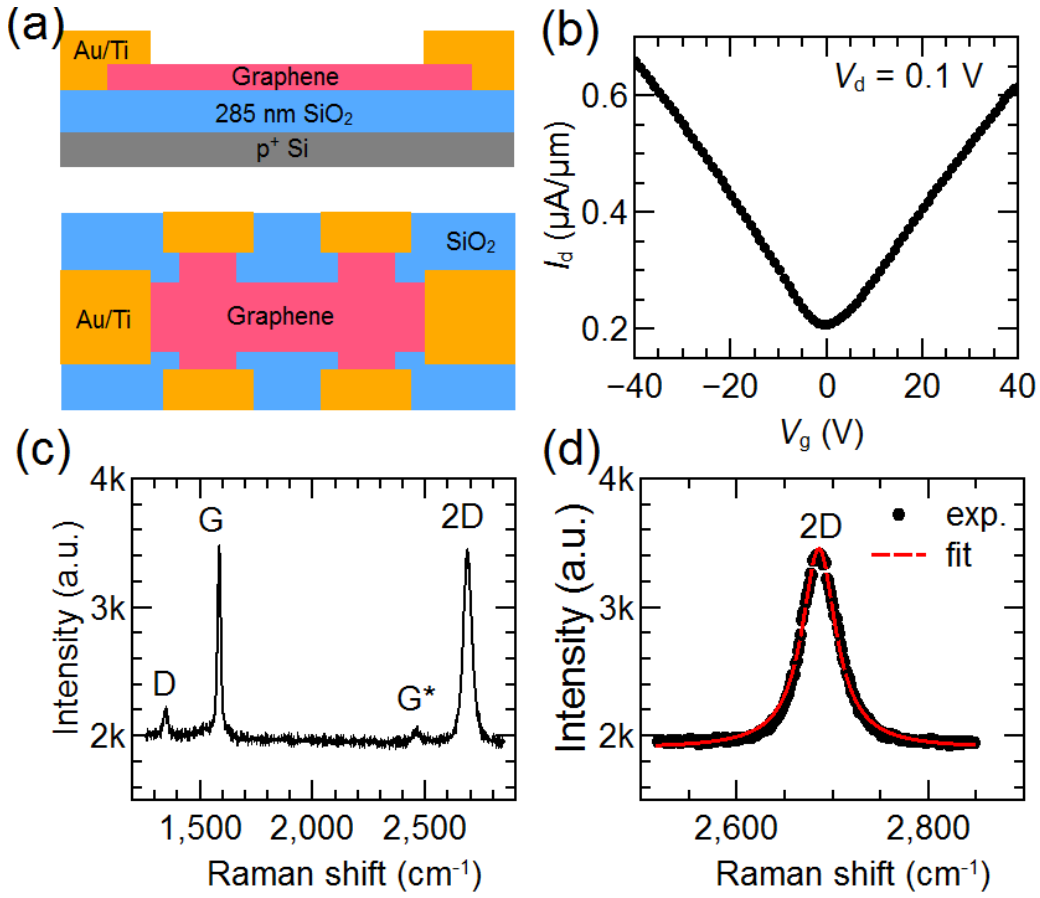

Figure 2.2 Characterization of graphene and device quality. (a) Schematic structure of the fabricated graphene Hall bar device. (b) Transfer characteristics of the device at a drain bias V_d of 0.1 V at 100 K. (c) Typical Raman spectrum of the graphene channel. The laser wavelength and power were 532 nm and 0.75 mW/cm^2, respectively. (d) 2D peak of graphene fitted with Lorentzian distribution.

2.3 Self-assembly of MNP arrays

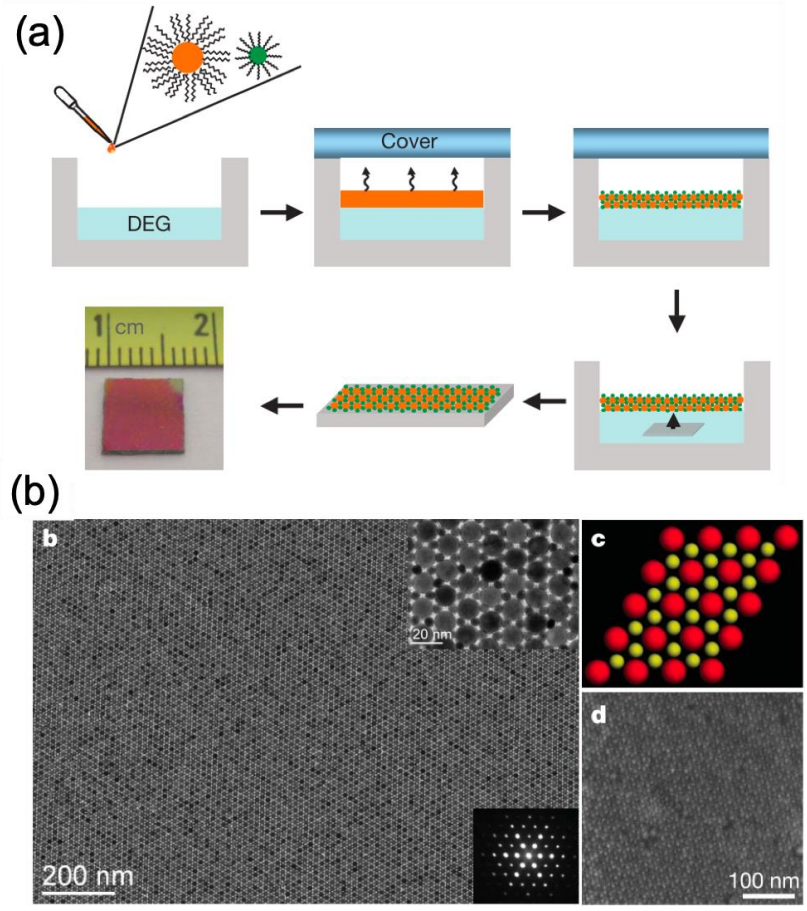

Figure 2.3 An example of self-assembly of MNP arrays using drop-casting technique in previous research [40]. (a) Process flow of self-assembling binary nanocrystal supperlattices (BNSLs) at liquid-air interface. (b) TEM image of the self-assembled BNSLs. Imaged adapted from Ref.[40].

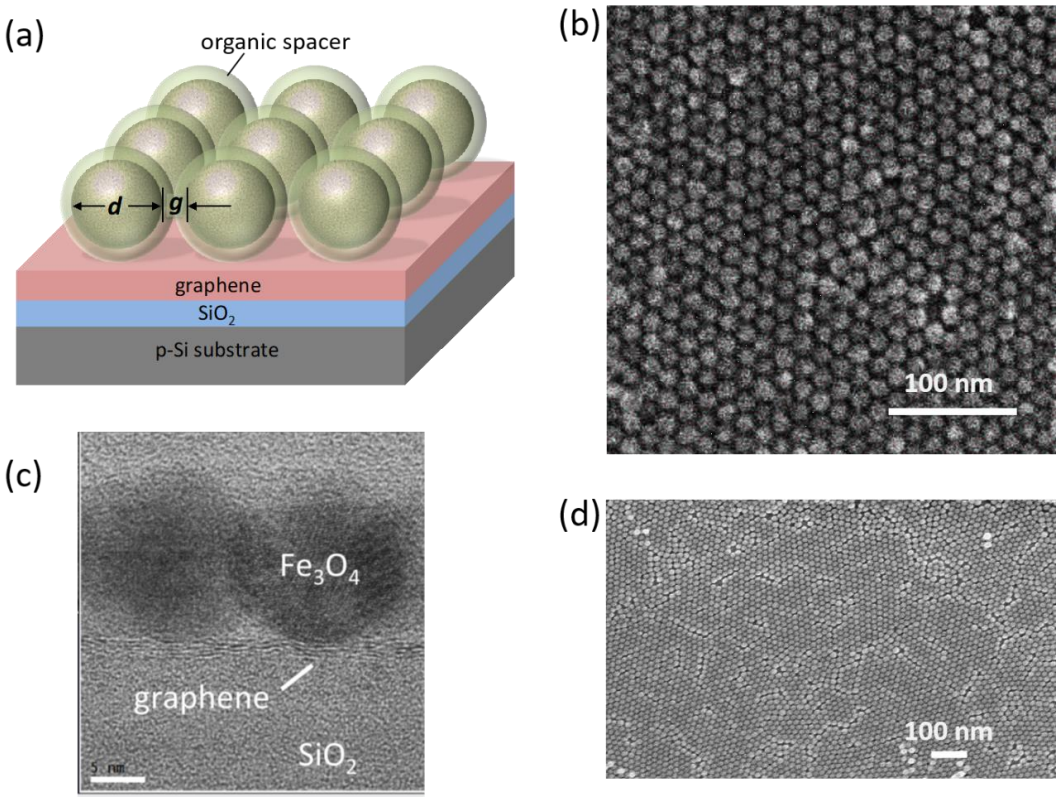

Figure 2.4 Fe_3O_4 MNP array self-assembled on graphene substrate. (a) Schemetic structure, (b) and (d) SEM images and (c) TEM image.

Fe_3O_4 nanoparticles arrays were formed on different types of substrates, including substrates containing pre-fabricated devices, using a liquid-air-interface self-assembly technique following the method of Dong *et al.* [40]. The process flow is shown in Figure 2.3 with an example TEM image. A 10-µl hexane solution (2 mg/ml) of 15-nm Fe_3O_4 nanoparticles, which is commercially available, was dropped on ethylene glycol (EG) surface in a Teflon well (1 inch in diameter) in which the desired sample sits on the bottom of the well. The well was covered by a glass slide leaving a small gap between Teflon and glass, allowing the hexane to evaporate slowly through the gap. After complete evaporation of hexane in about 1.5 minutes, an Fe_3O_4 nanoparticle array is

formed on the EG liquid surface. To transfer the nanoparticle array onto the sample surface, the EG was removed slowly using a pipette, allowing the nanoparticle array to be collected on the sample surface. Subsequent drying in a vacuum chamber overnight was used to remove the residual EG. This self-assembly method is not sensitive to the sample surface, thus can be used on various substrates and even on the pre-fabricated devices. The topology of the nanoparticles on graphene substrate and on pre-fabricated devices were then confirmed by SEM, as shown in Figure 2.4 and Figure 2.5. The intimate contact between the Fe_3O_4 cores and graphene after annealing was also supported by the TEM images of the interface, as shown in Figure 2.4c.

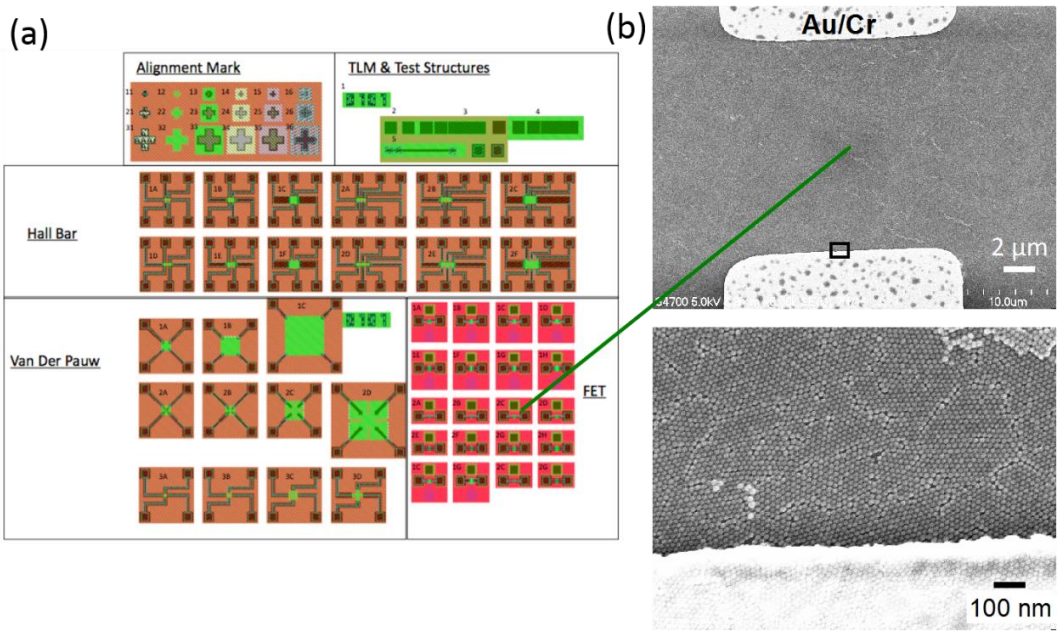

Figure 2.5 Fe_3O_4 MNP array self-assembled on fabricated graphene devices. (a) device map of the chip design. (b) SEM images of well aligned MNP array formed in large area on device surface.

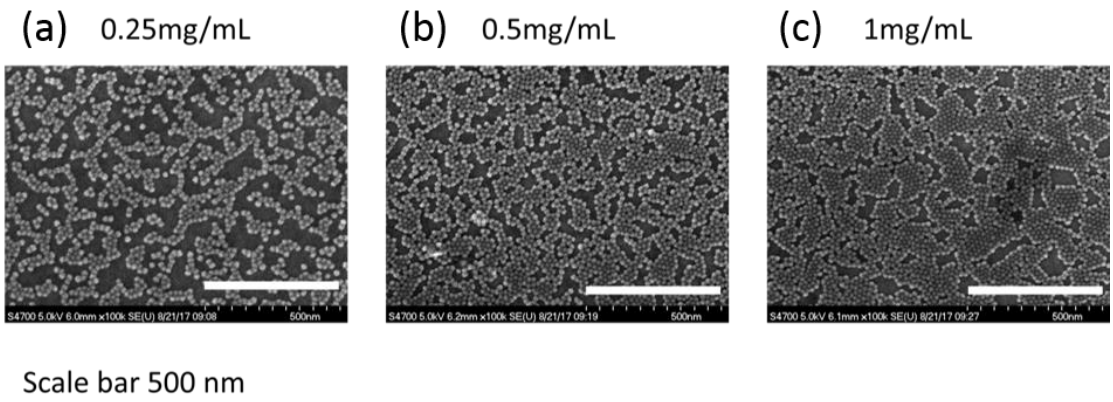

Figure 2.6 SEM images of Fe_3O_4 MNP layer on graphene using dip-coating method using nanoparticle solution with different concentrations. The scale bar is 500 nm.

For depositing nanoparticles with various surface coverage, I employed another dip-coating technique by dipping the sample in Fe_3O_4 nanoparticles solution with different concentrations (0.25, 0.5, 1 mg/ml) for 10 seconds and then dried the sample in air. The SEM images in Figure 2.6 show the increase of nanoparticle surface coverage with increasing the concentration of nanoparticle solution. The domain size of nanoparticle array is found to be ~100 nm for the 1mg/mL solution, which can be further improved by optimizing the concentration and dipping time. This method provides a simple and quick way to deposit nanoparticles on a sample surface with different surface coverage.

2.4 Shell removal for MNPs by annealing

To obtain the contact between Fe_3O_4 cores and graphene, annealing was performed to pyrolytically remove the organic shells of MNPs. The typical range of annealing conditions for sucessful shell removal are 250 to 300 °C for 30 min in nitrogen

gas or foming gas. After the annealing process, FTIR spectrum was taken to see whether the shell is removed by checking the peaks for alkyl C-H stretch as a signature for the oleic acid organic shell [41]. As shown in Figure 2.7, the peaks for alkyl C-H stretch disappeared after annealing, which indicates successful removal of the organic shells. To conclusively confirm the electrical contact between Fe_3O_4 cores and graphene, C-AFM images were taken before and after annealing. As shown in Figure 2.8, while MNPs are seen in both topographic AFM images, the current flow from the tip through the MNPs is only observable for the sample after annealing. This proves that the electrical contact between Fe_3O_4 cores and graphene is obtained by annealing, which is key understanding existence of PIFM in graphene, as discussed later.

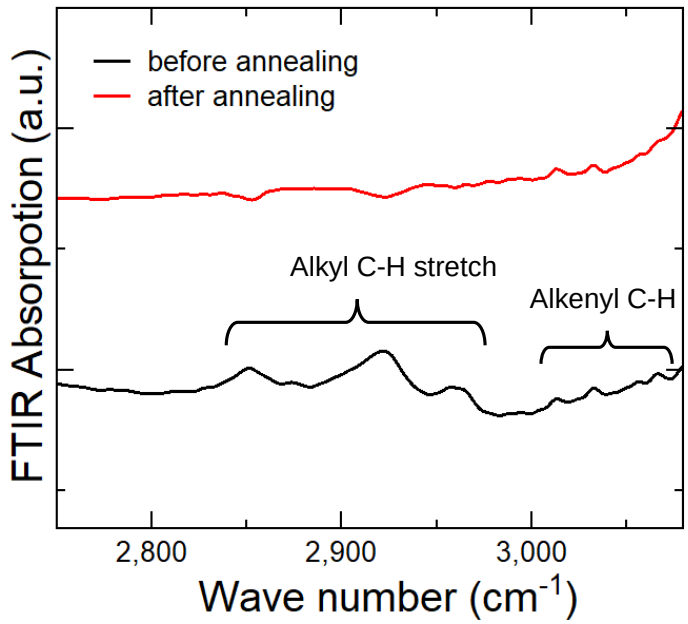

Figure 2.7 Comparison of FTIR spectrum for MNPs on graphene before and after annealing. The annealing was perform in forming gas at 300 °C for 30 minutes. The spectrum confirms the pyrolytic removal of the organic shells surrounding the MNP cores.

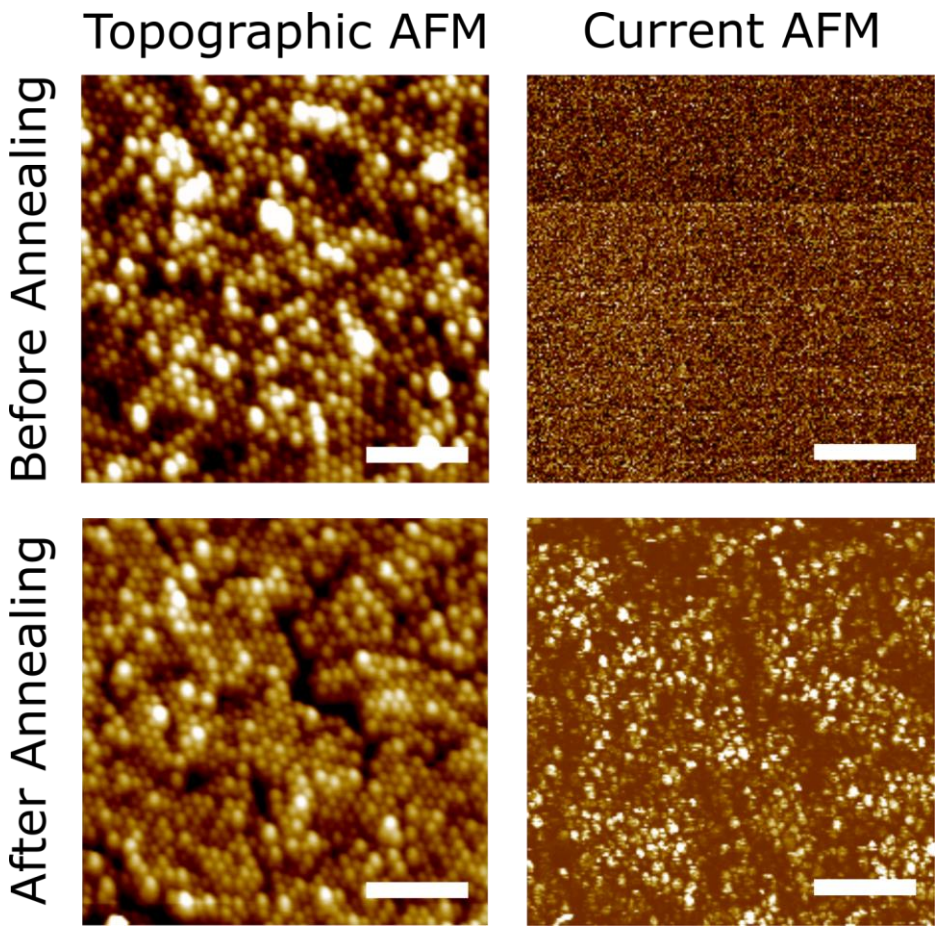

Figure 2.8 Comparison of AFM images for MNPs on graphene before and after annealing. The annealing was perform in nitrogen gas at 350 °C for 3 hours. Current between MNP and graphene is only observed for annealed samples confirming the successful removal of organic shells surrounding the MNP cores. Scale bar, 100 nm.

It is also important to show that there is no paralel current path in the MNP array layer for not shorting the graphene channel. I confirmed the electrical isolation between MNPs by electrical measruements, as shown in Figure 2.9. The facts that sheet resistivity ρ_s is comparable for both test and control samples and that no current (noise level) is detected for device with MNP array on SiO_2 (which means no graphene channel),

confirm that there is no parallel current path through the MNP array. Therefore, the gap between nanoparticles prevents the shorting of graphene channel.

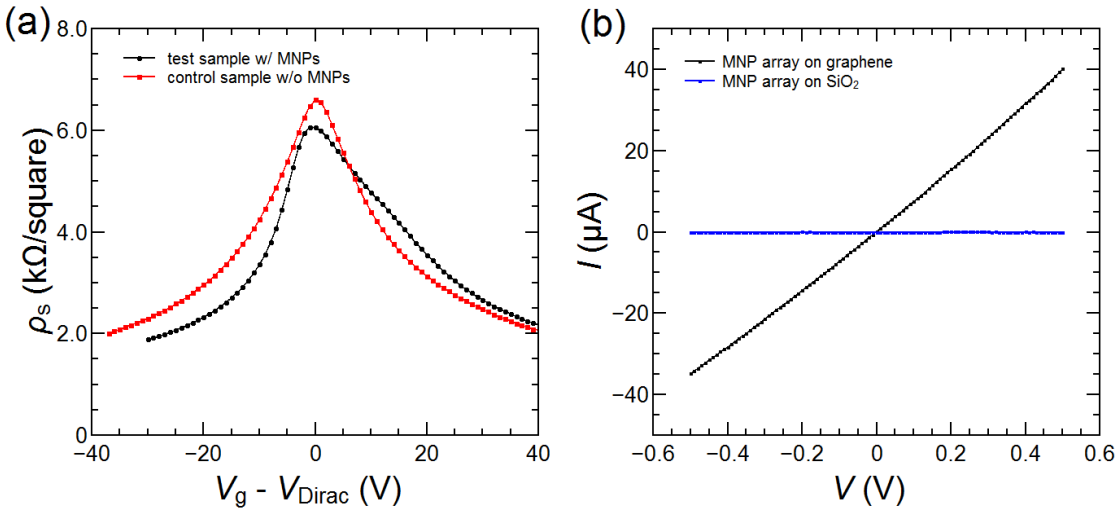

Figure 2.9 Confirmation of no parallel current path via MNP array. (a) sheet resistivity ρ_s as a function of gate bias point (V_g – V_{Dirac}) for a test sample with MNPs and for a control sample without MNPs. (b) *I-V* for both devices with MNP array on graphene and on SiO_2. In both figures, annealing was performed to remove the organic shells of MNPs.

2.5 Characterization of magnetization for MNP arrays

To study the magnetic properties of an MNP array, the field-dependent magnetization of the Fe_3O_4 MNP arrays on silicon substrate with native oxide was measured by VSM (Quantum Design) as a function of temperature. The VSM data in Figure 2.10a shows clear magnetic hysteresis. The rapid saturation characteristic for the in-plane field shows that the effective moment is preferably orientated in-plane, which is expected due to the dipole interactions within a monolayer (or thin layer) of MNPs. From the temperature dependence of the saturated magnetization M_s and the coercive

field H_c, a ferromagnetic to superparamagnetic transition is apparent. The blocking temperature T_B is about 150 K, as seen from the temperature where H_c goes to zero. M_s barely changes from 10 to 300 K since the Currie temperature T_C of Fe_3O_4 is ~ 850 K [42].

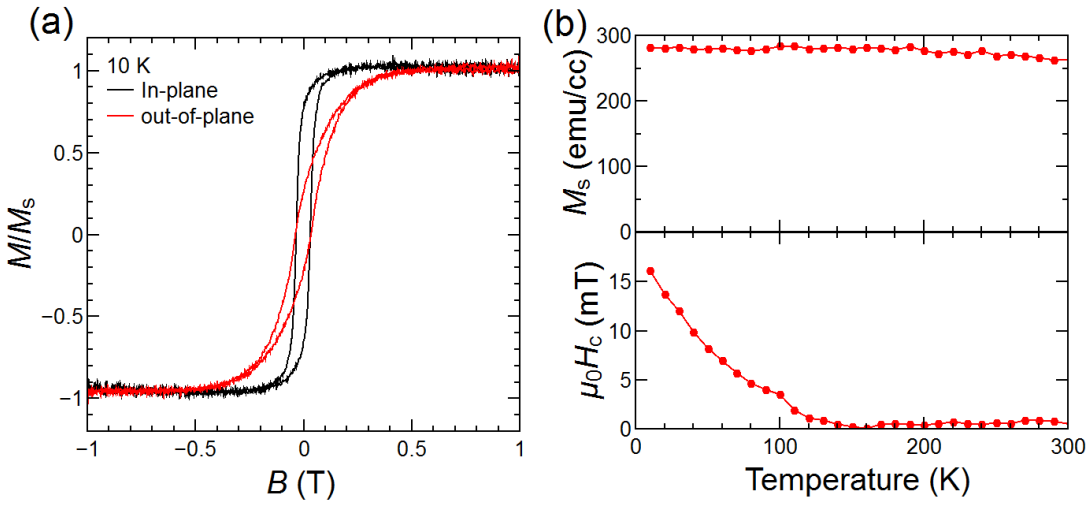

Figure 2.10 VSM characterization of Fe_3O_4 MNP array. (a) Normalized in-plane and outplane magnetic hysteresis curves at 10 K. (b) Extracted M_s and H_c as a function of temperature. The magnetic field is applied in-plane in (b).

2.6 Hall measurement system

The longitudinal resistivity ρ_{xx} and Hall resistivity ρ_{xy} were measured as a function of B and V_g by the van der Pauw method [43] under vacuum using a cryogenic Hall measurement system (Model 8425, Lake Shore Cryotronics) with a current source (Model 6220, Keithley) and a nano-voltmeter (Model 2182A, Keithley). Current-reversal averaging and geometry averaging techniques, as described in Ref.[44], were included to remove unwanted contributions due to offset currents and offset voltages. Back-gate bias V_g was applied to the p-Si substrate and the gate leakage current was monitored. The

magnetic field was applied perpendicular to the sample plane over the range of -2 to 2 T and the temperature of sample stage was varied from 10 to 300 K.

2.7 System set-up for STO measurements

Figure 2.11 is a photo of the system set-up for STO measurements. The system consists of a cryogenic probe station (Lake Shore), semiconductor parameter analyzer (Keysight B1500A), lock-in amplifier (Stanford Research, SR830), signal generator (Agilent), spectrum analyzer (Agilent) and source-meter modules (Keithley). These components can be connected in various ways for different measurements to detect STT and STO. The measurement ranges of the system are, from10 K to 400 K for temperature, from -2 to 2 T for magnetic field and up to 20 GHz for frequency. The high vacuum chamber is preferable for surface sensitive samples, like graphene devices.

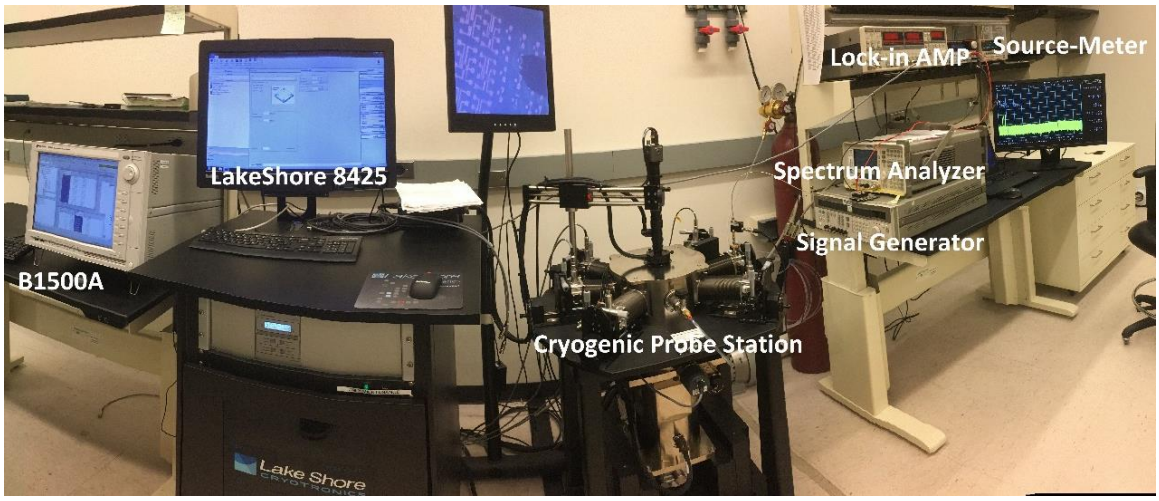

Figure 2.11 System set-up for STO measurements.

CHAPTER 3

TWO-CHANNEL TRANSPORT IN GRAPHENE AND MAGNETIC SENSORS

Graphene is a promising channel material for sensing magnetic fields via the Hall effect due to its atomic-scale thickness, ultra-high carrier mobilities compared to conventional semiconductor sensors. Because of its Dirac band structure, graphene sensors differ from semiconductor sensors in that both electrons and holes participate in the carrier transport. This two-channel transport complicates the sensor operation and causes performance trade-offs that demand careful examination. In this chapter, the operation of graphene sensors operated near the CNP where two-channel transport prevails is examined. A two-channel model is employed to explain the observation and to predict the sensor performance under linearity and power constraints. The work in this chapter has been published in *Commun. Phys.* **2**, 65 (2019) [45].

3.1 Introduction of graphene for magnetic field sensors

Studies of graphene for both magnetoresistance (MR) [12,13,46] and Hall sensors [16–18] have demonstrated performance outpacing traditional magnetic sensors based on semiconductors. For example, a large MR ratio of ~2000% at 9 T has been demonstrated in multilayer graphene on hexagonal Boron Nitride (h-BN) [46]. An even larger MR ratio of 55,000% at 9 T was obtained in extraordinary magnetoresistance devices, where the geometrical MR is enhanced by an embedded metal structure [12,13]. A record value of current-related sensitivity S_I of 5700 V/AT has been reported [16] for a graphene Hall sensor, which is nearly two orders of magnitude higher than that of commercial Silicon

Hall sensors (~100 V/AT) [47] and twice as high as that for the best two-dimensional electron gas (2DEG) based Hall sensors [48]. This record value was achieved in a structure comprised of exfoliated graphene and h-BN stacks designed for high mobility. S_I values in the range of about 1000 to 3000 V/AT have been reported for more practical structures based on CVD deposited graphene transferred onto various insulators, including exfoliated h-BN [16], CVD h-BN [7] and SiO_2 [8,17]. Advanced "encapsulated" designs based on an all-CVD h-BN/graphene/h-BN sandwich structure have also been reported [10], but have been limited thus far to about 100 V/AT due to high carrier densities, emphasizing the importance of obtaining low carrier density, in addition to high mobility, for high sensitivity.

3.2 Motivations and approaches

The MR ratio, sensitivity and linearity of graphene sensors are closely related to the presence of both electrons and holes near the CNP. The existence of a CNP is a unique feature of graphene's Dirac-cone band structure and distinguishes graphene sensors from conventional semiconductor-based sensors. Despite the general interest and demonstrated promise of graphene-based sensors, there has been little detailed investigation of the magnetoresistance characteristics and sensor performance of graphene near the CNP, which is essential for optimizing graphene sensor operation.

Here I present a study of the potential performance and optimization of graphene-based MR and Hall sensors. The study is based on a two-channel model that combines the longitudinal and Hall resistivities of parallel electron and hole channels with electrostatic carrier density expressions for graphene. The primary focus is the

optimization at biases near the CNP (i.e. the Dirac point), where the transport is complicated by the presence of both electrons and holes. I begin from validating the model by examining the experimental characteristics of sensors based on commercial CVD graphene transferred to a SiO_2/p-Si substrate over wide ranges of gate bias V_g, magnetic field B, and temperature T. It is shown that the experimental MR-B, Hall resistivity ρ_{xy}-B and ρ_{xy}-V_g characteristics are well-described by the model, including nonlinearities and unusual gate-bias dependence in the ρ_{xy}-V_g characteristic near the CNP. I use the model to extract carrier mobilities and densities and show that model agrees with experimental data over wide ranges in gate bias and magnetic field. The characteristics are also examined over a wide temperature range (10 to 300 K). I then make use of the validated model to study the optimization of the sensitivity, linearity and MR ratio and to estimate the realizable performance in high-quality graphene. Of particular interest in the results are trade-offs due to the linearity constraints of an application, which are especially important at high mobilities and high magnetic fields – a regime mostly neglected in prior works.

3.3 Two-channel model

Two-carrier magnetoresistance expressions were used to analyze the experimental data and to predict optimized performance. For a single carrier, longitudinal resistivity ρ_{xx} and Hall resistivity ρ_{xy} are given by:

for electrons,

$$\rho_{xx} = \frac{1}{en\mu_e}, \tag{3.1}$$

$$\rho_{xy} = \frac{B}{en}; \tag{3.2}$$

for holes,

$$\rho_{xx} = \frac{1}{ep\mu_{\mathrm{h}}}, \tag{3.3}$$

$$\rho_{xy} = \frac{B}{ep}; \tag{3.4}$$

where e is the elementary charge and n, p, μ_{e}, μ_{h} represent carrier densities and mobilities for electrons and holes, respectively. For parallel electron and hole channels with equal mobilities, ρ_{xx} and ρ_{xy} are given by:

$$\rho_{xx} = \frac{1}{e}\frac{(p+n)(1+(\mu B)^2)}{\mu((p+n)^2+(\mu B)^2(p-n)^2)}, \tag{3.5}$$

$$\rho_{xy} = \frac{1}{e}\frac{B(-p+n)(1+(\mu B)^2)}{((p+n)^2+(\mu B)^2(p-n)^2)}. \tag{3.6}$$

While for a single carrier ρ_{xx} is independent of B, equation (3.5) shows that ρ_{xx} is dependent on B^2 for two carriers of comparable density. Therefore, a large MR ratio is possible near the CNP. While for a single carrier ρ_{xy} depends linearly on B and tends to infinity as the carrier density approaches zero, equation (3.6) shows that ρ_{xy} depends nonlinearly on B for two carriers of comparable density and tends to zero as the net carrier density approaches zero. Therefore, the linearity and sensitivity of a graphene Hall sensor are strongly influenced by two-carrier transport.

For simplicity in discussing the model, I have given the expressions in the case of $\mu_{\mathrm{e}} = \mu_{\mathrm{h}}$ in equations (3.5) and (3.6), whereas the expressions for unequal mobilities [46] were used in the fitting analysis presented later (Figures 3.1 to 3.4). Examination of the expressions for unequal mobilities reveals that the deviations from the single carrier case

occur when the two channels have comparable conductivities [46], not comparable densities. Nevertheless, the deviations occur near the CNP even for unequal mobilities due to the strong dependence of carrier densities on gate bias. Near the CNP, inhomogeneities may occur due to charge impurities, intrinsic structural wrinkles and substrate roughness[49,50]. It is believed that the resulting random potential fluctuations in the channel modulate the Dirac-cone band structure so strongly that interspersed electron and hole puddles form, as has been observed experimentally[51,52]. Various theoretical treatments have been proposed to provide a detailed understanding of transport in this situation[49,53–55]. A simple physical picture[55,56] is that the carriers move along percolation paths while scattering from puddle interfaces. Since the puddles are larger than the mean free path, the conductivities of individual puddles can be described by drift-diffusion[55], and the transport involves a longer effective path-length and additional scattering (higher resistance). Thus, although puddles complicate the physical picture at the CNP and modify the effective transport parameters, the two-channel model still provides a useful approximation and has been used successfully for the study of graphene sensors by several groups[17,46,53].

To develop a simple theory i) for checking the accuracy of the electron and hole densities extracted from the data in the analysis and ii) for predicting the performance of MR and Hall sensors, we combined the two-carrier magnetoresistance expressions [46] with electrostatic carrier density expressions [57] for the gate-bias dependent electron and hole carrier densities in graphene, similar to that done by Chen *et al.* [17]. The key relationships in the electrostatic carrier density expressions are:

$$n_{\mathrm{tot}} = p + n \cong \sqrt{n_0^2 + n[V_{\mathrm{g}}]^2}, \tag{3.7}$$

$$n\left[V_{\mathrm{g}}\right] = p - n = -\frac{C_{\mathrm{ox}}}{e}(V_{\mathrm{g}} - V_{\mathrm{CNP}}); \tag{3.8}$$

where n_{tot} is the total carrier density, n_0 is the minimum carrier density at the CNP, $n\left[V_{\mathrm{g}}\right]$ is the gate-bias dependent net charge density, C_{ox} is the gate capacitance and V_{CNP} is the gate bias at the charge neutrality point. In contrast to Chen *et al*, who used a simplified model assuming that $\mu B << 1$, we use the full two-carrier resistivity equations above. This allows us to study performance trade-offs due to linearity constraints and to predict the sensor performance for high-quality graphene (high μ and low n_0) and high magnetic fields.

3.4 Magnetic field dependence of magnetoresistance and Hall resistivity

3.4.1 Experimental

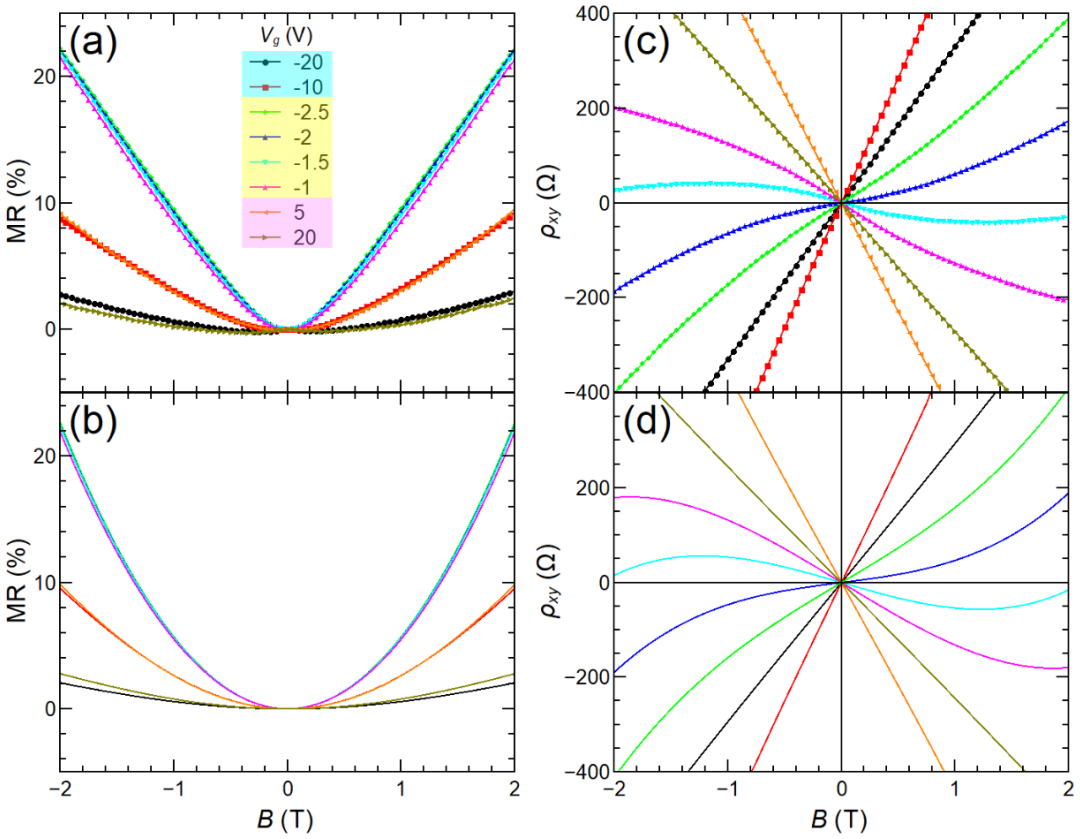

Figure 3.1 Dependence of magnetoresistance MR ratio and Hall resistivity ρ_{xy} on magnetic field B for various values of gate bias V_g. MR-B at various V_g: (a) experimental data and (b) modeled results. ρ_{xy}-B at various V_g: (c) experiment data and (d) modeled results. Good agreement is obtained between the experiment and model over wide ranges in V_g and B. The color bands in this figure and Figure 3.2 indicate hole dominated (light blue), electron dominated (pink) and two-carrier (yellow) regions. (The current and temperature for these and the other experiments were 1 μA and 100 K, respectively, unless stated otherwise.)

Figure 3.1a shows the variation of the MR ratio, which is defined as $\{\rho_{xx}(B) - \rho_{xx}(0)\}/\rho_{xx}(0)$, as a function of magnetic field B for different gate biases V_g. The current and temperature for these and the other experiments were 1 μA and 100 K, respectively, unless stated otherwise. For the biases farthest from the CNP (V_g = -20 and 20 V), where one carrier dominates (holes or electrons, respectively) the MR ratio is very small, as expected from the Drude model of single carrier transport. It can be seen that the highest MR ratio is achieved at V_g close to the CNP (V_g = -2.5, -2, -1.5 and -1 V) where both carriers are present. (Note: the V_g values in Figure 3.1 were chosen symmetrically around the CNP (V_{CNP} = -1.7 V), causing the hole and electron data to overlap.) The MR ratio at 2 T and 100 K is ~22%, which is comparable to that previously reported for graphene at the same field and temperature [46].

Figure 3.1b presents the calculated MR ratio using the two-channel model. It is important to note here that the calculated MR agrees well with the experimental data, except that the experimental data is more linear at high fields. Such linearity has been attributed to electron-hole recombination leading to an edge conductivity contribution [58,59].

A highly linear ρ_{xy}-B characteristic is critical for many Hall sensor applications. Figure 3.1c shows the Hall resistivity ρ_{xy}-B at various V_g. It can be seen that the linearity of ρ_{xy} degrades when the gate bias is close to the CNP (V_g = -2.5, -2, -1.5 and -1 V). Following Xu *et al.* [8], linearity error α is defined as $(\rho_{xy} - \rho_{xy}^0)/\rho_{xy}^0$, where ρ_{xy}^0 is the best linear fit value of the ρ_{xy}-B curve. I define α_{max} as the maximum of α over the B range. In the electron or hole dominated regimes (V_g = -20 and 20 V), the value of α_{max} for the

data is very low, less than 2%. However, α_{max} increases rapidly as V_g approaches the CNP, reaching a value of 77% at V_g = -2 V, which means ρ_{xy} is not linearly dependent on B in the two-carrier regime.

Close examination of the dependence of the ρ_{xy}-B characteristic on V_g shown in Figure 3.1c reveals another type of unusual behavior near the CNP. The rotation of the curves around the origin with increasing V_g changes direction near the CNP – i.e., the rotation is clockwise near the CNP (the slope ρ_{xy}/B decreases with V_g from -10 to +5 V) while it is counter-clockwise away from the CNP (the slope ρ_{xy}/B increases with V_g for $|V_g| > \sim 10$ V). In the analysis below, it will be shown that this unusual rotation reversal behavior is also a result of two-carrier transport.

3.4.2 Modeling

To examine whether the nonlinearity and rotation effects in Figure 3.1c can be explained by two-carrier transport, I fit the MR-B and ρ_{xy}-B data in Figure 3.1a and c simultaneously with the two-carrier magnetoresistance expressions in equations (3.5) and (3.6). The fitting parameters were the electron and hole mobilities, which were taken to be independent of V_g, and the carrier densities, which were taken to be dependent of V_g.

Calculated results for the two-channel model using the extracted parameters are in close agreement with the experimental results as shown in Figure 3.1b and d. However, the validity of the model also requires that the extracted mobilities and densities are accurate. The extracted electron and hole mobilities are 2598 and 2168 cm^2/Vs, respectively, which are reasonable values for commercial quality graphene on SiO_2/p-Si substrates. It is also important to examine the extracted carrier densities in order to

validate the model. While the extraction of carrier density from Hall data is simple for a single charge carrier, the presence of two carriers makes the extraction difficult. Nevertheless, we find that the extracted values of electron and hole density are also reasonable throughout the entire gate-bias range, as shown in Figure 3.2. (The theoretical curves in Figure 3.2 will be discussed later.).

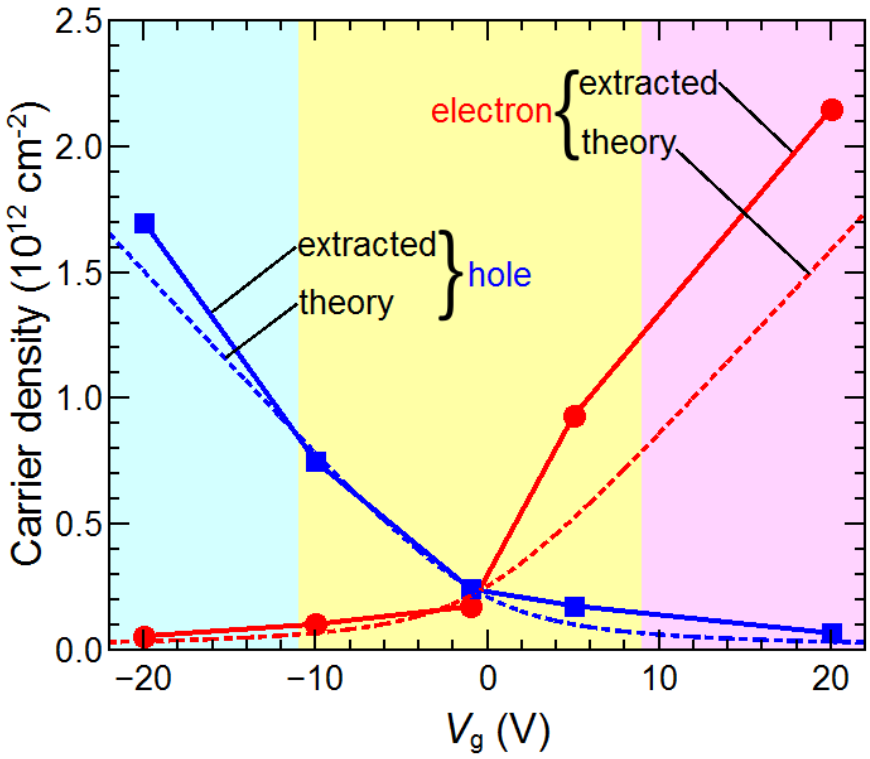

Figure 3.2 Comparison of the electron and hole densities i) extracted by fitting the two-carrier magnetoresistance expressions to the experimental data and ii) calculated from the electrostatic carrier density expressions. The extracted densities (solid) and calculated densities (dashed) as a function of V_g are in good agreement with each other, which is important for validation of the model.

3.5 Gate-bias dependence of Hall resistivity and current related sensitivity

3.5.1 Experimental

Here we experimentally examine the influence of two-carrier transport on the Hall sensitivity. The current-related sensitivity S_I is defined as $V_{xy}/IB = \rho_{xy}/B$ [47]. Two-carrier transport near the CNP will affect S_I through its impact on the ρ_{xy}-V_g characteristic. The variation of ρ_{xx}, ρ_{xy} and S_I with V_g is shown in Figure 3.3. The increase in ρ_{xx} with increasing B near the CNP shown in Figure 3.3 is due to two-carrier transport. Figure 3.3b shows that $|\rho_{xy}|$ peaks on either side of the CNP and that ρ_{xy} crosses zero at the CNP. This is different from the case of a single carrier, where ρ_{xy} is proportional to the inverse of the carrier density and therefore tends to infinity as the carrier density approaches zero. In graphene, however, the total carrier density ($p + n$) does not approach zero. Instead, ($p + n$) reaches a minimum value n_0 and the net density ($p - n$) changes sign at the CNP. This peaking of $|\rho_{xy}|$ places an important limitation on the realizable sensitivity and affects the optimum bias condition for a graphene Hall sensor, as will be considered in detail later. While the temperature for the data presented in this section was mainly 100 K, the ρ_{xx}-V_g and ρ_{xy}-V_g characteristics were examined over a range in temperature from 10 to 300 K and confirm the excellent thermal stability of graphene Hall sensors [8], as discussed next.

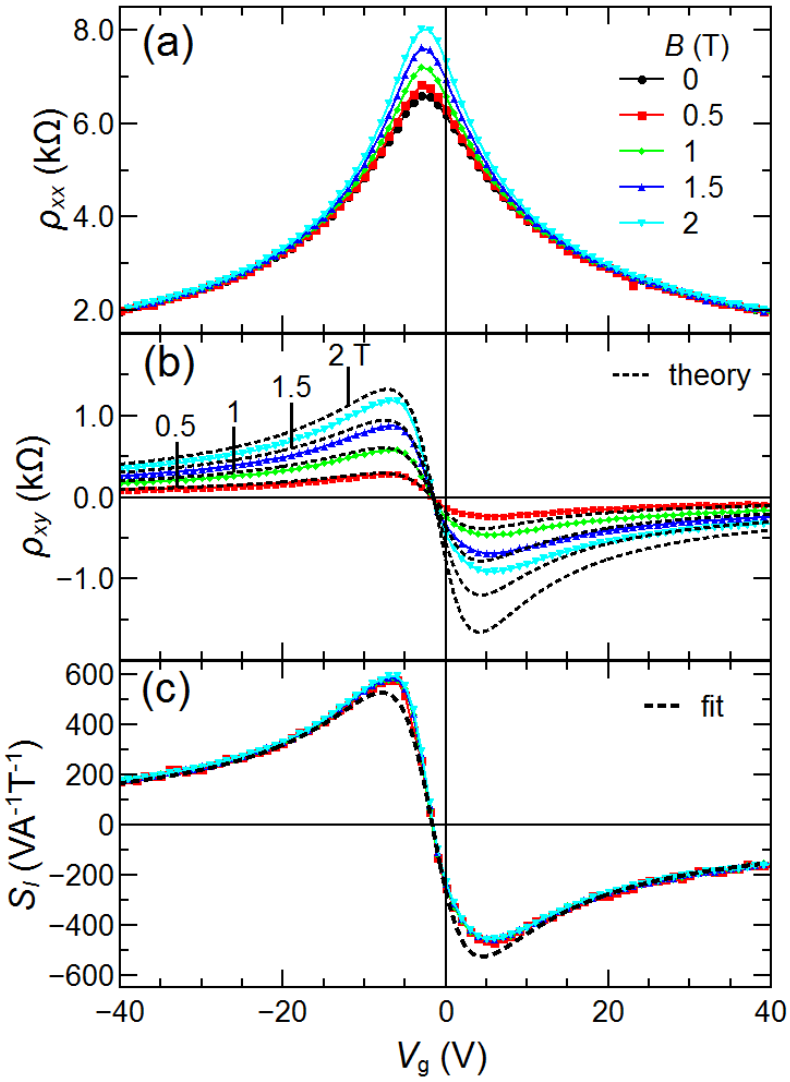

Figure 3.3 V_g dependence of the resistivities (a) ρ_{xx}-V_g and (b) ρ_{xy}-V_g and the current-related sensitivity (c) S_I-V_g for various B. The dashed lines in (b) are theoretical characteristics calculated from the model, which show good agreement with the experiment, especially on the left side of the CNP. The dashed line in (c) shows the fit to the data that was used to extract the residual carrier density n_0 used in the model. The peaking of $|\rho_{xy}|$ places a limitation on sensitivity and affects the optimum bias condition.

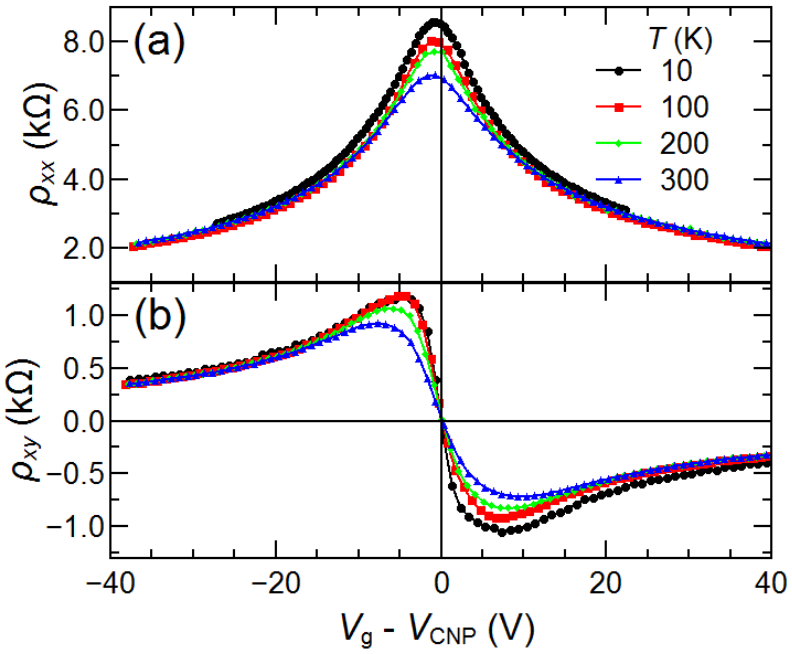

Figure 3.4 Temperature dependence of resistivities. Experimental results for (a) ρ_{xx} vs $V_g - V_{CNP}$ and (b) ρ_{xy} vs $V_g - V_{CNP}$ for B = 2 T at various temperatures from 10 to 300 K.

An important factor for Hall sensor applications is the dependence of ρ_{xy}/B and, hence, S_I on operating temperature [8]. I performed measurements for ρ_{xx} and ρ_{xy} vs ($V_g - V_{CNP}$) over a wide temperature range, and the results are shown in Figure 3.4a and b. The figures show that an increase in temperature results in a decrease in the peak value of $|\rho_{xx}|$ at the CNP and a shift of the peaks in $|\rho_{xy}|$ away from the CNP. These temperature dependences are consistent with the thermal spreading of the carrier distribution due to Fermi-Dirac statistics. The decrease in the peak ρ_{xy} is attributed to the increase in n_0 with increasing temperature [17]. The maximum value of ρ_{xy} in Figure 3.4b is 928 Ω at 300 K, which corresponds to S_I = 464 V/AT. This sensitivity is comparable to the room-

temperature values of semiconductor Hall sensors, which are about 100 and 700 V/AT for Si and GaAs sensors [47], respectively.

It is also interesting to note that the S_I behavior in Figure 3.3c indicates that ρ_{xy}/B decreases with increasing V_g near the CNP (V_g from -7 to +5 V) while it increases with increasing V_g away from the CNP, which is consistent with the conclusion that the rotation reversal in Figure 3.1c is the result of two-carrier transport.

3.5.2 Modeling

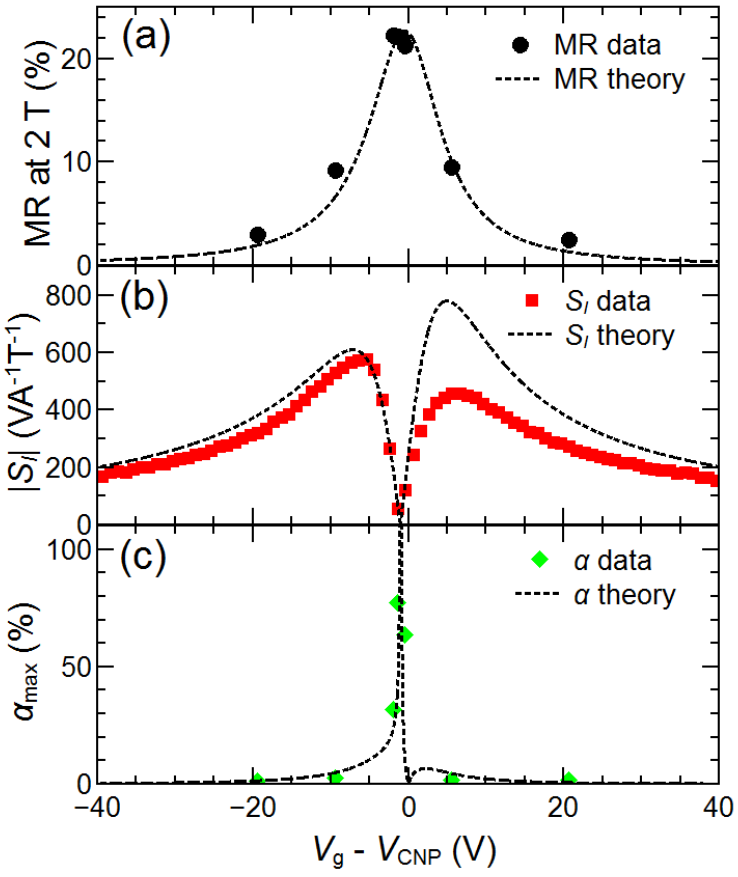

Figure 3.5 Comparison of experimental (dots) and theoretical (dashed lines) sensor performance for (a) MR, (b) $|S_I|$ and (c) maximum linearity error αmax as a function of $V_g - V_{CNP}$.

To test the capability of the model for predicting MR and Hall sensor performance I attempted to fit the experimental data over wide ranges in gate voltage and magnetic field. Following Peng *et al*. [17], n_0 was extracted by fitting the S_I-V_g characteristic in Figure 3.3c. The extracted $n_0 = 4.65 \times 10^{11}$ cm^{-2} was then used to calculate the electron and hole densities as a function of V_g using the electrostatic carrier density expressions in equations (3.7) and (3.8). The calculated densities are plotted along with the experimental values in Figure 3.2 and are seen to be in good agreement with the experiment. From the calculated densities and extracted mobilities, I worked backwards to calculate theoretical ρ_{xy}-V_g characteristics for various B, which are plotted along with the experimental data in Figure 3.3b. Working backwards in a similar way, the theoretical MR, S_I and α_{max} characteristics were determined and are plotted along with experimental results in Figure 3.5. The agreement between the theory and experiment in Figure 3.3b and Figure 3.5b is excellent, except near the peak on the electron-side. (The better agreement on the hole side of the characteristics simply reflects the better fit obtained on the hole side in Figure 3.2.). The agreement shows that the model should be useful for estimating the optimized performance of graphene Hall sensors over wide ranges in mobility and magnetic field.

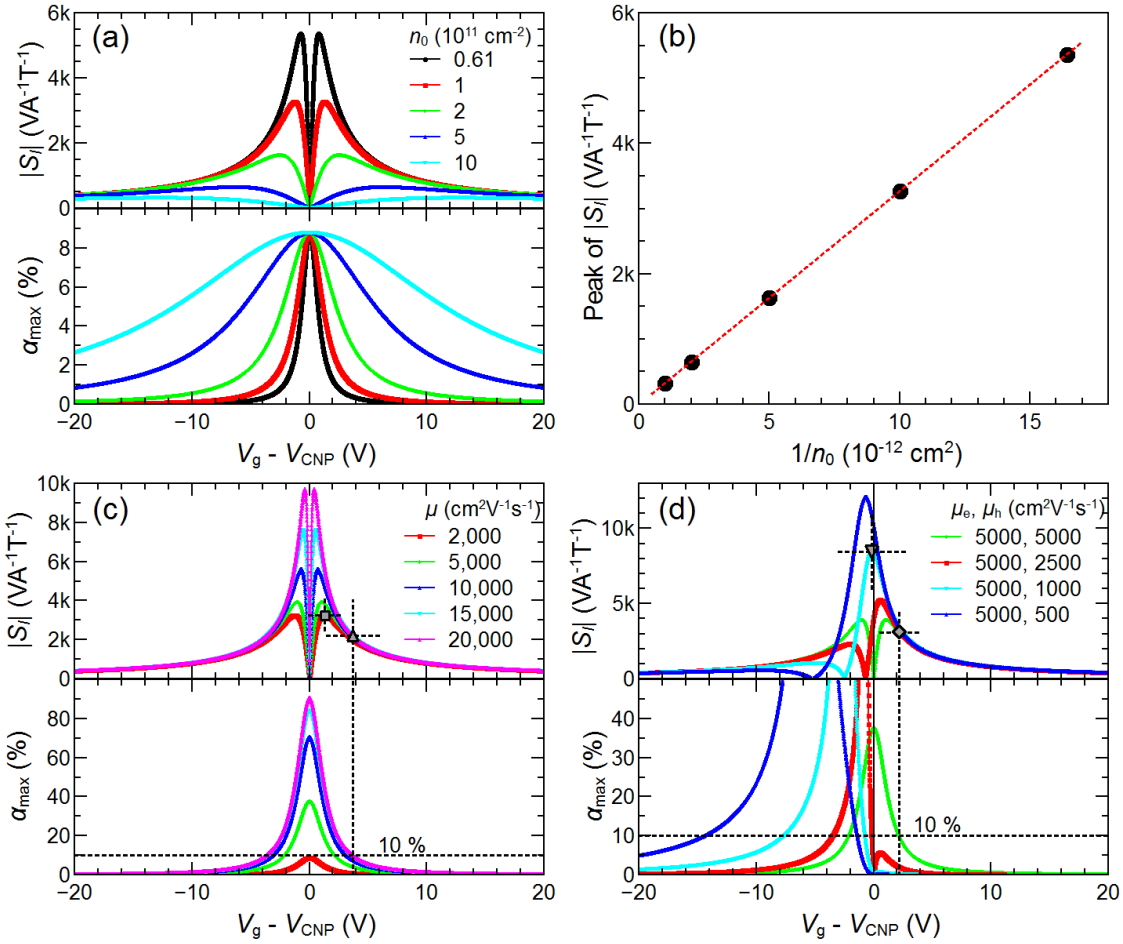

Figure 3.6 The influence of material-quality parameters μ and n_0 on current-related sensitivity and linearity. (a) Modeled $|S_I|$ (top) and α_{max} (bottom) vs $V_g - V_{CNP}$ at various n_0 for μ = 2000 cm^2/Vs, B = 2 T, (b) $|S_I|$ vs 1/n_0, as extracted from (a), (c) modeled $|S_I|$ (top) and α_{max} (bottom) vs $V_g - V_{CNP}$ for equal electron and hole mobilities ($\mu_e = \mu_h = \mu$) and (d) modeled $|S_I|$ (top) and α_{max} (bottom) vs $V_g - V_{CNP}$ for unequal electron and hole mobilities ($\mu_e \neq \mu_h$) for $n_0 = 1 \times 10^{11}$ cm^{-2}, B = 2 T. Symbols in (c) and (d) show the realizable S_I for α_{max} = 10% for different mobilities. The modeling shows that the realizable S_I values, which are inversely proportional to n_0, are reduced by linearity constraints.

3.6 Dependence of modeled current-related sensitivity and MR ratio on residual carrier density and mobilities

I now use the model to explore the influence of material-quality parameters (μ and n_0) on sensitivity, linearity and MR ratio for graphene magnetic sensors.

3.6.1 S_I vs V_g for diffirent n_0

Figure 3.6a shows modeled results for n_0 over the range 6.1×10^{10} to 1×10^{12} cm^{-2} with μ and B set equal to 2000 cm^2/Vs and 2 T, respectively. (The lower limit of n_0 was chosen to be equal to the theoretical thermal limit at 300 K [17].) It is seen that n_0 has a strong influence on the peak value of S_I, which occurs at about 1 V on either side of the CNP and reaches a value of 5360 V/AT as n_0 decreases to 6.1×10^{10} cm^{-2}. As depicted in Figure 3.6b, the peak S_I is proportional to $1/n_0$, which agrees with Chen *et al.*'s conclusion in previous work [17]. The peak value of α_{max} occurs exactly at the CNP and reaches a value 8.8% independent of n_0, while the width of the α_{max} decreases with decreasing n_0. Since α_{max} is proportional to $(\mu B)^2$ [47], the linearity is improved at lower B. Thus, both higher sensitivity and higher linearity occur for lower n_0. At this moderate mobility, α_{max} is always low enough that operation at the peak S_I point is possible. However, for high mobilities the strong variation in both S_I and α_{max} with V_g introduces an important performance trade-off, which we examine next.

3.6.2. S_I vs V_g for diffirent μ

Figure 3.6c shows results for μ over the range of 1000 to 20,000 cm^2/Vs for n_0 and B set equal to 1×10^{11} cm^{-2} and 2 T, respectively. It is seen that the peak values of both S_I and α_{max} increase with increasing μ. Since increased S_I is beneficial while increased α_{max} is not, this represents a performance trade-off. Because of this trade-off, the peak S_I cannot be realized and is limited to a value that depends on the α_{max} constraint; we call this realizable value S_I^R. For example, if α_{max} is constrained to 10% and μ = 2000 cm^2/Vs, then Figure 3.6c shows that S_I^R occurs at 1.3 V (square symbol), which is the peak of S_I and is equal to 3270 V/AT. On the other hand, for the same α_{max} but μ equal to 20,000 cm^2/Vs, S_I^R occurs at 3.7 V (triangle symbol), which is away from the peak S_I, and is therefore limited to only 2180 V/AT. At this operating point, $|S_I|$ is only about 20% of its peak value of 9730 V/AT. The reason behind this counterintuitive effect (viz., that increased mobility can degrade S_I^R) and its implications will be considered later.

3.6.3 S_I vs V_g for different μ: Effect of non-equal μ

In the above examples, the electron and hole mobilities were assumed to be equal. Figure 3.6d shows results for carrier mobility ratios μ_h/μ_e over the range of 1 to 1/10. As can be seen from Figure 3.6d, decreasing μ_h while keeping μ_e constant causes the peak S_I to increase and shift to the left while α_{max} decreases near the peak (both desirable). In the case of μ_h/μ_e = 1000/5000, for example, the peak S_I is about 2 times that for equal mobilities while the α_{max} at the peak is 1% compared to 22% for equal mobilities. These changes in the S_I and α_{max} characteristics result in an improvement in S_I^R of nearly 3 times

for α_{max} = 10% (see symbols in Figure 3.6d). The reason for this improvement is that the transport for a higher mobility ratio is more similar to that for a single carrier, where S_I tends to be high while α_{max} is low. It is interesting that a difference in carrier mobilities can have a significant influence on both S_I and α_{max} as well as the optimum V_g bias point. The impact of this on performance will also be considered in a later section.

3.6.4 MR vs V_g for different n_0 and μ

I have also used the model to explore how the MR ratio is affected by μ and n_0. Figure 3.7a shows the modeled results for MR-V_g when n_0 is varied from 6.1×10^{10} to 1×10^{12} cm^{-2} with μ and B set equal to 2000 cm^2/Vs and 2 T, respectively. Contrary to what was seen for S_I in Figure 3.6a, the peaks of MR occur exactly at the CNP. While the peak MR value is independent of n_0, a larger n_0 gives a wider peak and hence a larger V_g operating range. Figure 3.7b shows the calculated MR for μ varied from 1000 to 20,000 cm^2/Vs with n_0 and B set equal to 1×10^{11} and 2 T, respectively. The MR peak value increases dramatically with μ, reaching nearly 1600% as μ approaches 20,000 cm^2/Vs, a mobility representative of that for high-quality graphene on h-BN [60,61]. Figure 3.7a and b show that, in contrast to Hall sensitivity, the key to achieving high MR ratio in graphene is having a high μ rather than a low n_0.

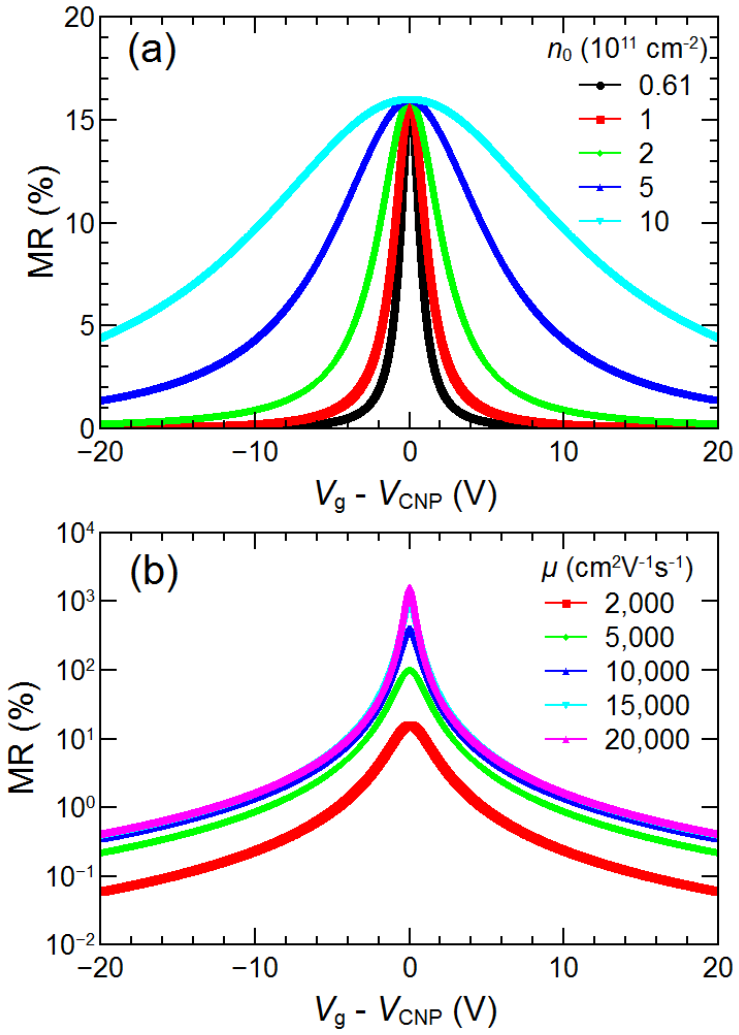

Figure 3.7 The influence of material-quality parameters μ and n_0 on MR ratio. (a) Modeled MR vs $V_g - V_{CNP}$ at various n_0 for μ = 2000 cm^2/Vs, B = 2 T and (b) modeled MR vs $V_g - V_{CNP}$ for various mobilities ($\mu_e = \mu_h = \mu$) for $n_0 = 1 \times 10^{11}$ cm^{-2}, B = 2 T. The modeling shows that the key to achieving a high MR ratio in graphene is having a high μ, rather than a low n_0.

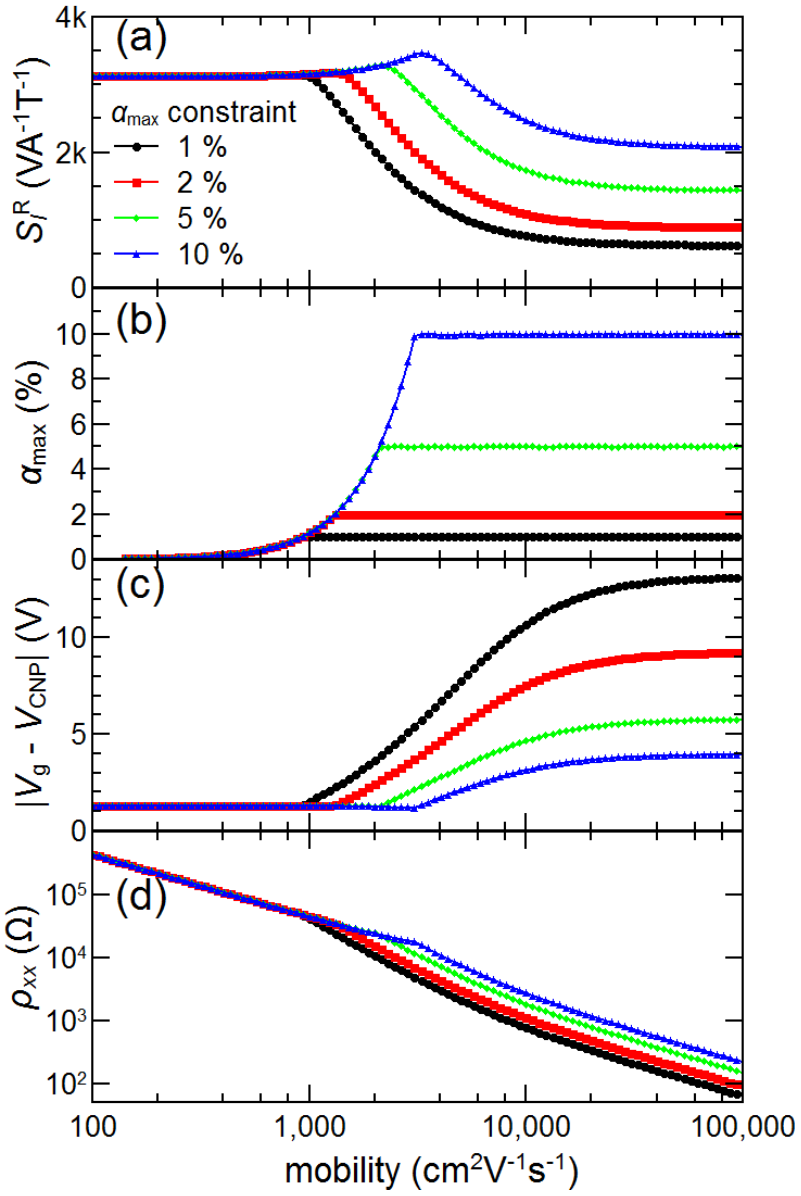

Figure 3.8 Dependence of realizable current-related sensitivity on mobility and linearity. Modeled (a) S_I^R, (b) α_{max}, (c) $|V_g - V_{CNP}|$ and (d) ρ_{xx} vs mobility for various α_{max} constraints for $n_0 = 1 \times 10^{11}$ cm^{-2} and $B = 2$ T. V_g is optimized for the highest S_I^R within the α_{max} constraints. These results show the interplay between the linearity constraint and mobility in determining the realizable S_I values; in particular a stringent linearity constraint together with a high mobility results in a substantial reduction in S_I^R.

3.7 Dependence of realizable sensitivities on mobility and linearity and power constraints

Here we examine the details of how a linearity constraint influences the realizable current-related sensitivity S_I^R, as well as the absolute sensitivity $S_A = V_{xy}/B = S_I I$. S_A is proportional to $(\mu/n_s)^{1/2} P^{1/2}$,[47] where n_s is sheet carrier density and P is power, and thus S_A the most important parameter for power-limited applications. The realizable value of S_A, which we refer to as S_A^R, is constrained by both the needed linearity and the power limitation for the particular application.

The linearity constraint affects the S_I^R at high mobility values, as illustrated in Figure 3.8a and b, which show S_I^R and α_{max} vs μ at B = 2 T for various constraints on α_{max} (1, 2, 5 and 10%). As shown in Figure 3.8b, the α_{max} constraint is active for mobilities above a critical value, which we define as μ_c. For example, the value of μ_c for α_{max} = 10% is 3270 cm^2/Vs. It can be seen in Figure 3.8a that S_I^R is near its maximum value of 3470 V/AT when μ is less than about 1000 cm^2/Vs for all shown values of α_{max}. However, increasing the mobility above 1000 cm^2/Vs results in an α_{max}-dependent decrease in S_I^R. This is because the operating bias must be moved further away from the CNP to meet the α_{max} constraint when $\mu > \mu_c$, as is shown in Figure 3.8c. While S_I^R barely changes when μ is lower than 1000 cm^2/Vs, the channel resistivity ρ_{xx} at the operating bias increases rapidly with decreasing μ to values too high for low-power operation, as illustrated in Figure 3.8d. At a higher resistivity the maximum current I_{max} is power-limited at a lower value.

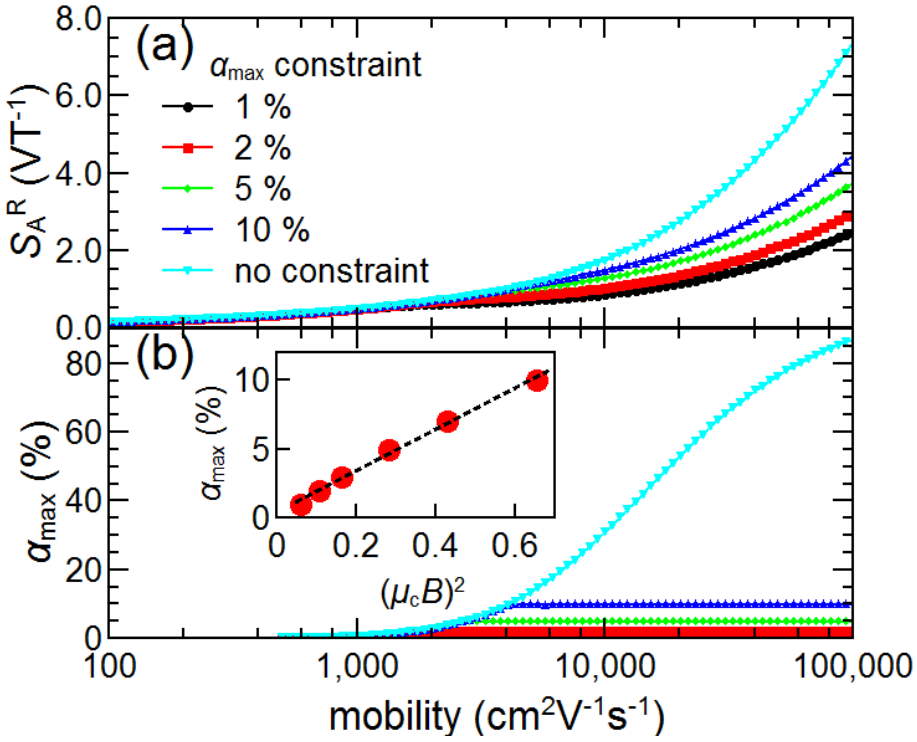

Figure 3.9 The dependence of realizable absolute sensitivity on mobility and linearity. (a) Modeled S_A^R and (b) α_{max} vs mobility for various α_{max} constraints for $n_0 = 1 \times 10^{11}$ cm^{-2}, $B = 2$ T and $P = 1$ mW. V_g is optimized for the highest S_A^R within the α_{max} constraints. The inset shows the dependence of α_{max} on $(\mu_c B)^2$, where μ_c is determined from the break points in (b) and dashed line is a linear fit. The results show that, when mobility is higher than μ_c, the linearity constraints substantially reduce S_A^R comparing to the unconstrained case.

Although S_I^R is commonly used as a figure of merit of Hall sensors, S_I^R does not take power into account. Thus, S_A^R, which depends on both linearity constraints and power limitations, is a better figure merit for power-limited applications. Figure 3.9a and b show S_A^R and α_{max} vs μ for various α_{max} constraints values (1, 2, 5, 10%; and unconstrained) with an assumed power limitation of 1 mW. In contrast to S_I^R, which decreases for higher mobilities, we can see that S_A^R increases monotonically with μ.

However, the linearity constraints greatly reduce S_A^R compared to the unconstrained case in the high mobility regime when $\mu > \mu_c$. For example, the value of μ_c for α_{max} = 10% is 4040 cm^2/Vs. At μ = 20,000 cm^2/Vs, for instance, α_{max} constraints of 1 and 10% lead to reductions of S_A^R by 58 and 27%, respectively, compared with the unconstrained value. The results in Figure 3.9a show that an S_A^R of 4.5 V/T at 1 mW (equivalent 0.14 V/T at 1 μW) should be possible for high-quality graphene with good linearity over a large magnetic field range (α_{max} = 10%, B = 2 T, $n_0 = 1 \times 10^{11}$ cm^{-2}, μ = 100,000 cm^2/Vs).

3.8 Discussion

Several points about the results presented above deserve further discussion. Since α_{max} is proportional to $(\mu B)^2$ [47], the calculated results for B = 2 T in Figures. 3.5 through 3.8 can easily be extended to other B values. In the insert of Figure 3.9b I have plotted α_{max} vs $(\mu_c B)^2$, as determined from the data in Figure 3.9. As shown in the figure, for $(\mu_c B)^2$ less than 0.65, α_{max} is less than 10%, which indicates that S_A^R is not limited by a 10% linearity constraint; while for larger $(\mu B)^2$, S_A^R is reduced for a 10% linearity constraint. As was seen in the calculations, higher mobility and higher magnetic field result in poorer linearity, which limits S_I^R and S_A^R to lower values. Thus, determining μ_c for the α_{max} and B demanded by a particular application can be useful in designing graphene Hall sensors, especially in the high mobility and high magnetic field regimes.

As was seen in Figure 3.8a, S_I^R is near its maximum value for μ below about 1000 cm^2/Vs. This does not mean that a low mobility is sufficient for good sensor performance since power limits must also be considered in many applications. S_A^R is the relevant figure-of-merit for power-limited applications and lower mobility limits S_A^R to

lower values. The advantage of graphene for achieving high S_A^R is that it offers both high mobility and low sheet carrier density. For example, for a simple graphene-on-SiO_2 structure with μ and n_0 values of 7800 cm^2/Vs and 1×10^{11} cm^{-2} [17], respectively, the equivalent S_A^R value based on the reported S_I and current-voltage data is 0.9 V/T at a power of 1mW with a linearity error of 4% for B = 0.4 T. This S_A^R value, which is slightly lower than the calculated value of 1.4 V/T for the same parameters, is the best reported result for this simple structure. For an advanced h-BN encapsulated, exfoliated graphene [16] structure, record sensitivity values of S_V = 2.8 V/VT and S_I = 5700 V/AT have been reported, which correspond to an equivalent S_A^R value of 4.0 V/T at 1mW. Although neither the linearity nor the mobility were reported with this record data, we can use the model to estimate the sensitivity and linearity by assuming μ = 80,000 cm^2/Vs (the mobility reported for similar h-BN encapsulated CVD graphene [60]) and n_0 = 1×10^{11} cm^{-2} (a typical value for high quality graphene). The model shows that an equivalent S_A^R of 4.0 V/T at 1 mW should be possible with α_{max} = 10% for B up to 2 T. If we increase μ to 120,000 cm^2/Vs, the best value reported near room temperature in exfoliated and suspended graphene [62], then S_A^R increases by about 20% to 4.9 V/T at 1 mW. Thus, the model indicates that the record experimental S_A^R reported for advanced graphene Hall structures is 80% of what can be achieved with good linearity (α_{max} = 10%). If excellent linearity (α_{max} = 1%) is required, however, the model indicates that a value of 2.8 V/T is the best that can be expected.

An important part of this study has been to take into account how the linearity constraint of an application influences the achievable performance of a graphene Hall

sensor. The basic issue is that, even though graphene offers high mobility with low residual carrier density at biases near the CNP (both beneficial for Hall sensing), linearity is reduced because of comparable conductivities for the electron and hole channels in this bias regime. Thus, schemes for providing that one channel conductivity dominates over the other could be useful for improving linearity. The obvious approach of biasing the device away from the CNP so that the density of one carrier dominates can improve linearity, but seriously degrades sensitivity due to the increased carrier density. However, the alternative scheme of reducing the mobility of one carrier compared to the other does not suffer from this drawback. While electron and hole mobilities in graphene are usually similar, carrier mobility ratios of ~0.3 have been reported for graphene FETs [63,64] and attributed to asymmetric scattering for electrons and holes [64]. Higher ratios might be possible in engineered structures. Calculated results on the effect of the mobility ratio μ_h/μ_e on Hall sensor sensitivity and linearity were presented in Figure 3.6d, where it can be seen that S_I^R improves by a factor of nearly 3 for $\mu_h/\mu_e = 0.2$ and $\alpha_{max} = 10\%$. In the power-limited case, the calculations show that an improvement in S_A^R of about 50% is possible under the same assumptions. Another scheme for providing that one conduction channel dominates over the other is to use an electrical contact technology having different contact resistances for electrons and holes. Previous studies have reported electron-hole conduction asymmetry for various metal/graphene contacts [65–67], and this effect might also be engineered to improve Hall sensor linearity.

It is important to realize that although the two-carrier nature of graphene is a disadvantage for linearity, this does not mean that graphene is inferior to single-carrier

semiconductor Hall sensors. The calculations for graphene with $n_0 = 1 \times 10^{11}$ cm^{-2} give an S_I^R of 3470 V/AT with 10 % linearity, which is comparable to the best experimental S_I^R value of 2745 V/AT reported for graphene on SiO_2 [17]. These values are much higher than those for Si and GaAs sensors [47]: 100 and 700 V/AT, respectively. The calculations for high-quality graphene ($n_0 = 1 \times 10^{11}$ cm^{-2}, μ = 100,000 cm^2/Vs, α_{max} = 10%, B = 2 T, P = 1 mW) give S_A^R = 4.5 V/T which is about 2 times higher than the best values reported for narrow-gap III-V heterostructure sensors (S_I = 2750 V/AT; S_A = 2.17 V/T at 1 mW) [48]. Thus, graphene provides performance much better than simple semiconductor structures and comparable to the best complex III-V heterostructure designs.

3.9 Conclusion: Graphene Magnetic Sensors

I have presented an experimental and theoretical study of graphene magnetoresistance and Hall sensors biased near the charge neutrality point, where the presence of both electrons and holes dominates the characteristics. Experiments were used to validate a two-channel model, which was then used to explore the influence of gate bias V_g, carrier mobility μ and residual density n_0 on performance over a wide range in magnetic field B. Careful attention was paid to the linearity of the Hall characteristics and sensitivities near the CNP.

The results of the model show that linearity constraints reduce both the realizable current-related sensitivity S_I^R and the absolute sensitivity S_A^R when the mobility is above a critical value μ_c, which scales with B. When the mobility is increased above μ_c, the linearity constraint causes S_I^R to decrease and S_A^R to increase at a lower rate. When linearity constraints and power limitations are considered, and the gate bias is optimized,

the achievable sensor performance for high-quality graphene is S_A^R of 4.9 V/T for a linearity of 10% with B up to 2 T at a power of 1 mW. Thus, in addition to its promise for realizing simple, low-cost Hall sensors with excellent temperature stability, graphene offers sensor performance far beyond that of simple semiconductor structures and comparable to that of advanced III-V heterostructure designs.

CHAPTER 4

PROXIMITY INDUCED FERROMAGNETISM IN GRAPHENE FROM MNP ARRAYS

In this chapter, I present the observation of AHE in the MNP/graphene device structure, which provides the signature of PIFM. Side-by-side comparison of the test samples with different control samples conclusively prove that the exchange interaction at the MNP/graphene interface is responsible for the observed AHE. The PIFM in graphene is shown to persist at room temperature and to be gate-tunable.

4.1 Introduction of graphene for spintronics

Graphene is a promising channel material for spintronics because of its long spin diffusion length and excellent electrical properties [2,3,50], including high carrier mobility and gate-tunable carrier concentration. Spin injection and transport in graphene has been widely studied in the past [19–23,68]. It has attracted much attention for making graphene magnetic for both scientific and technological interests [24]. Magnetic moments in graphene due to vacancy defects, adatoms and doping have been researched in both theoretical and experimental studies [2,24,25]. However, scattering caused by random impurities could greatly reduce the high carrier mobility of graphene, which is not desirable for graphene applications. Recently, PIFM in graphene from an FMI thin film has been achieved in several systems [26–29,69–73]. Proximity effect from an adjacent FMI provides a method to achieve ferromagnetism in graphene while preserving the transport properties of the graphene layer. It is necessary that parallel conduction does not short the graphene channel. FMI layer, including YIG [26,27] and EuS [28,29], have been used to

achieve PIFM in graphene. However, FMIs are limited in number and difficult to integrate with graphene, especially for high quality interface which is essential for proximity effect. An alternative method is to provide PIFM in graphene from isolated MNPs. This greatly expands the range of ferromagnetic materials from insulators to conductive semiconductors, semimetals and metals, thus i) it allows one to work with high quality, single domain nanoparticle structures and ii) it provides a simple and low-cost way to achieve PIFM in graphene for large scale applications.

MNPs comprised of a Fe_3O_4 cores coated with oleic acid shells can be self-assembled into a monolayer array in these experiments. Fe_3O_4 is a highly stable magnetic semiconductor with a high Curie temperature. The oleic acid shell provides a highly uniform spacer between the Fe_3O_4 cores in the array. While the Fe_3O_4 cores of the MNP are not insulating, the separation between cores in the array provides the needed insulation, rather than the material itself. In the following of this Chapter, I demonstrated PIFM in graphene from MNPs.

4.2 PIFM in graphene via anomalous Hall effect

AHE is a useful method to prove PIFM in graphene/YIG structure, as describe in Ref.[26]. Here I employed the same AHE to study PIFM in the MNP/graphene devices.

4.2.1 Hall measurements at different V_g

To study PIFM from MNP array, I fabricated Fe_3O_4 MNP/graphene structures as described in Chapter 2. Hall measurements at different gate bias V_g were performed on Hall bar devices without MNPs (control sample) and devices with MNPs (test sample). Annealing was performed to remove the organic shell of MNPs. Here I show the results

on test samples with low MNP density and annealed by rapid thermal annealing (RTA) for ~300 °C in forming gas for 30 minutes (see Chapter 2 for details), unless stated otherwise.

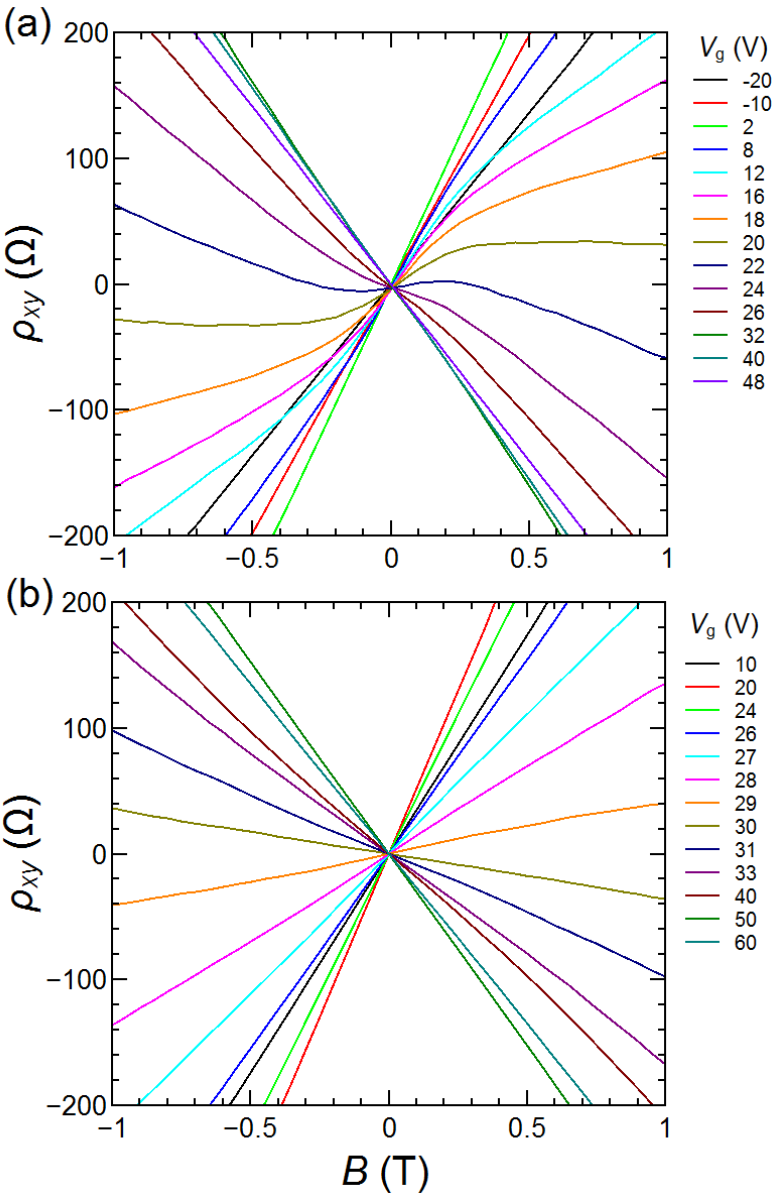

Figure 4.1 Comparison of Hall characteristics ρ_{xy}-B at various V_g between (a) MNP test sample and (b) control sample. Only MNP test sample shows nonlinearly Hall curves near the Dirac point, indicating the effect is from MNP. (The current and temperature for these and the other experiments were 1 μA and 10 K, respectively, unless stated otherwise.)

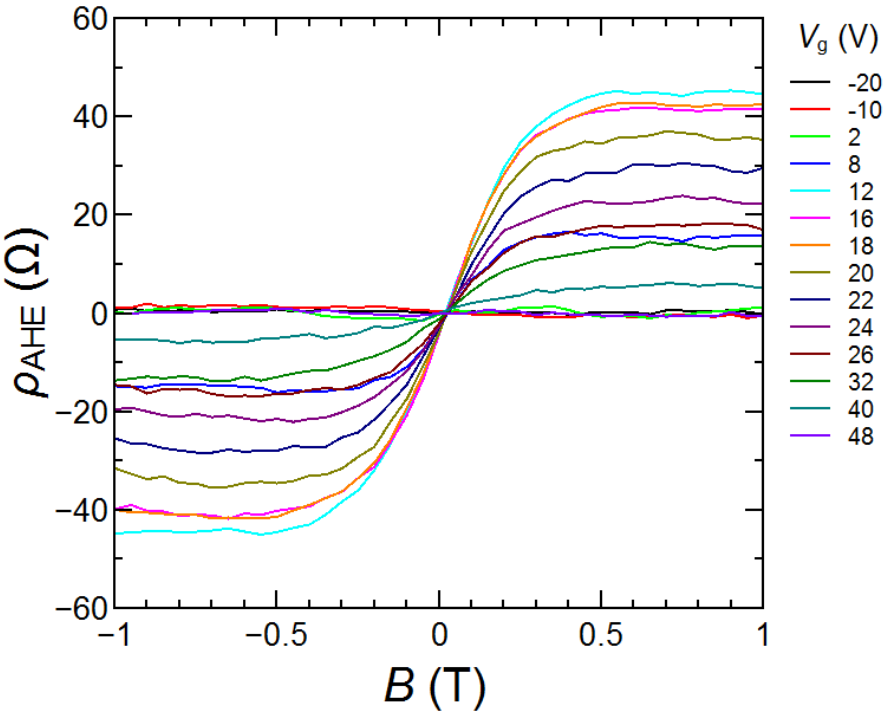

Figure 4.2 ρ_{AHE} characteristic extracted from Figure 4.1a. ρ_{AHE} shows a clear saturation above B = 0.5 T, which is an indication of the saturation of the magnetization of MNPs.

The test sample shows sharp nonlinearity in the ρ_{xy}-B characteristics at V_g near the Dirac point in contrast to the linear characteristics in the control sample which is simply due to the normal Hall effect, as shown in Figure 4.1. The fact that the characteristics for the two samples are virtually identical except for the nonlinearities provides evidence that the nonlinearity is not the result of parallel conduction through the array. Such parallel conduction would strongly alter the effective carrier density and mobility and, hence, drastically change Hall characteristics. Sheet resistivities for the two samples are nearly the same, which also confirms there is no parallel conduction via MNP array. The ~2-nm gaps between particles that are defined by the organic shells in the self-assembled MNP array. While the shells have been removed in the MNP sample by pyrolytic dissociation,

the gaps remain and thus prevent parallel shorting path in MNP array as discussed previously in Chapter 2.

As discussed in Chapter 3, a non-linear Hall characteristic for graphene near the Dirac point can come from two channel transport which can be fully modeled. Trying to fit the ρ_{xy}-B curves by the same two-channel model, I confirmed that the nonlinear Hall characteristics (Figure 4.1a) which shows sharp turning point and saturation cannot be fitted and explained by the two-channel model. PIFM is the possible explanation. In ferromagnets, Hall resistivity

$$\rho_{xy} = \rho_{\mathrm{H}}(B) + \rho_{\mathrm{AHE}}(M) = \alpha B + \beta M, \tag{4.1}$$

where $\rho_{\mathrm{H}}(B)$ is the ordinary Hall effect (OHE) term due to Lorentz force which is linearly dependent on B and $\rho_{\mathrm{AHE}}(M)$ is the AHE term which is proportional to M [74]. The saturation of the M-B characteristic in a magnetic material (thin film, MNP etc.) causes a saturation of $\rho_{\mathrm{AHE}}(M)$ and in turn gives a nonlinearity in the characteristic. The results of ρ_{xy}-B on the test sample tends to saturate at high B which makes it possible to subtract the linear OHE component and get the $\rho_{\mathrm{AHE}}(M)$. The resulted ρ_{AHE}-B shows a clear saturation when B reaches about 0.5 T and the saturated ρ_{AHE} is the highest at V_{g} near the Dirac point and reduces when V_{g} is biased away from the Dirac point, as shown in Figure 4.2. The decreasing of saturated ρ_{AHE} on V_{g} will be shown in detail later.

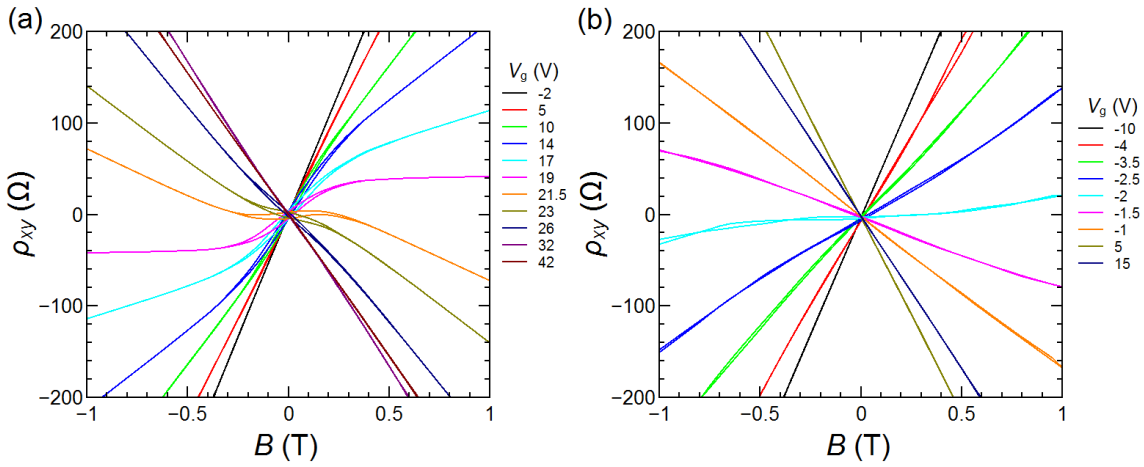

Figure 4.3 Loops of ρ_{xy}-B at various V_g for (a) MNP test sample and (b) control sample. Hysteres were only seen in MNP test sample for V_g near the Dirac point.

4.2.2 Comparison of Hall with magnetization characteristics

To check if ρ_{AHE} follows magnetization of the MNP array, I took ρ_{xy}-B loops to explore hysteresis as well as nonlinearity. Hysteresis is only seen in the test sample, as shown in Figure 4.3, not in the control sample, which gives evidence that the nonlinearity is magnetic related in nature. Then, I plot normalized ρ_{AHE} and M vs B and they agree well in both hysteresis and shape of the nonlinearity, showing the ρ_{AHE} follows the magnetization of the MNP array, as shown in Figure 4.4. Furthermore, the dependencies of coercive force H_C on temperature from magnetization and Hall characteristics are consistent, as depicted in Figure 4.5. (Note that the difference in H_C can be explained by the MNP density variation from sample to sample.)

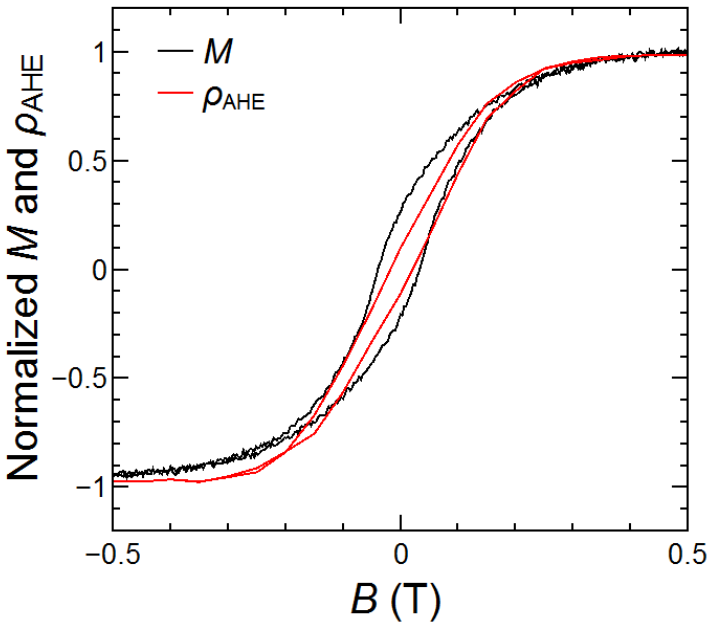

Figure 4.4 Comparison of the normalized ρ_{AHE}-B characteristic and M-B characteristic of an Fe_3O_4 MNP array, showing the graphene magnetoresistance closely follows the magnetization of the MNP array and exhibits a similar hysteresis chracteristics.

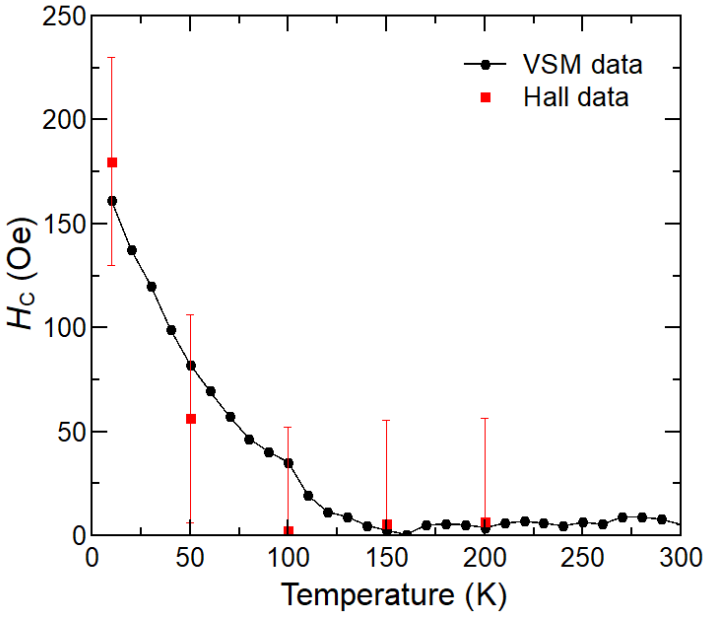

Figure 4.5 Comparison of coercive force H_C from VSM measurements and Hall measurements as a function of temperature.

4.2.3 Exchange interaction at MNP/graphene interface

However, one can still argue that the nonlinearity in ρ_{AHE}-B is simply from a magnetostatic (dipole) interaction between graphene and the MNP array, i.e. graphene is uncoupled from the MNP but is affected simply by a modification of the effective B-field in the graphene due to the nearby MNP. To check whether the nonlinearity is due to an exchange interaction at the MNP/graphene interface or not, I compared ρ_{AHE}-B for the test sample to two types of control samples: a sample with no MNP (sample A) and a sample that had MNPs but was not annealed (sample B). In the latter case, the MNPs are separated from the graphene by the 1-nm oleic acid shells. Figure 4.6 shows that the hysteresis and nonlinearity are only seen in the test sample, thereby confirming that these effects are due to atomic contact between the MNP and graphene. Thus, the interaction at MNP/graphene interface is an exchange interaction.

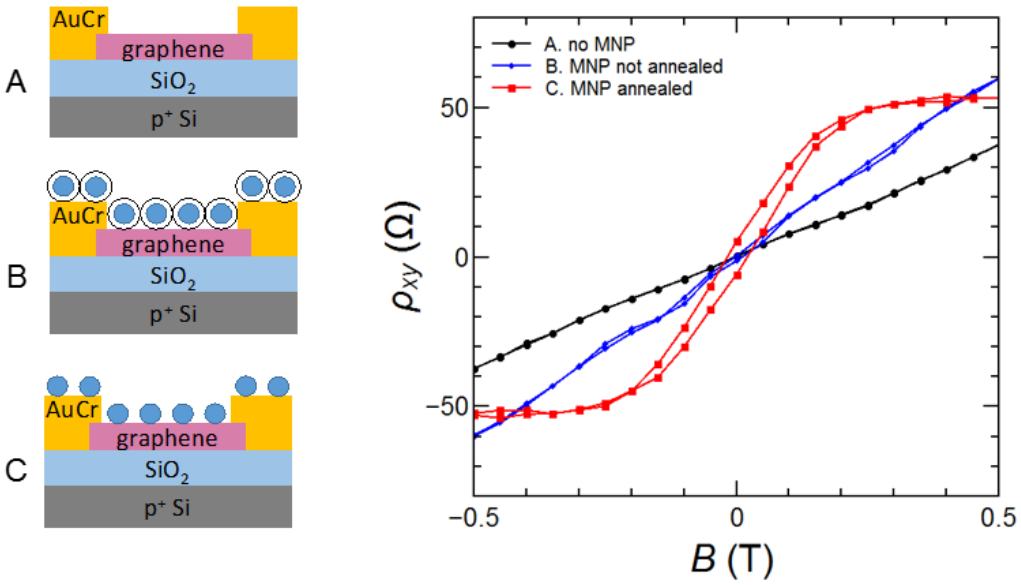

Figure 4.6 Comparison of ρ_{xy}-B characteristics for control and test samples: (A) no-MNP, (B) MNP not annealed, (C) MNP annealed, confirming that only the MNP annealed sample exhibits the nonlinearity and hysteresis signatures of PIFM.

4.2.4 Key points for achieving PIFM in graphene

To understand the key factors to achieve PIFM in MNP/graphene structure, I made a systematic variation of device fabrication parameters, including annealing environment, coverage of MNP and quality of graphene, and then did Hall measurements to investigate the AHE in these devices. For different annealing environment as shown in Figure 4.7, all tested samples show AHE. The annealing temperature and time were kept the same, 250 °C and 30 minutes, respectively. This indicates that the annealing environment is not critical to achieve PIFM if the annealing process is enough to remove the shells of MNPs.

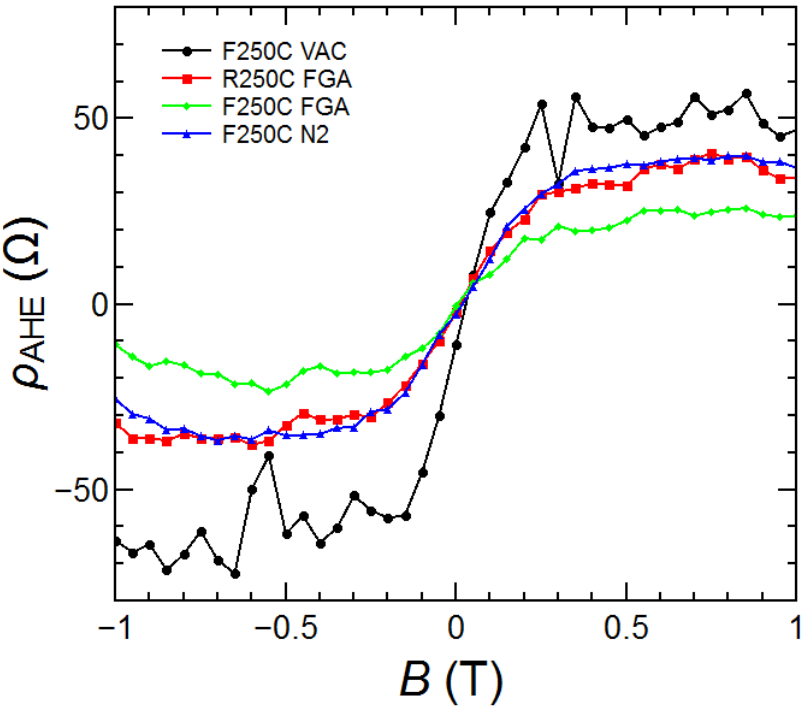

Figure 4.7 ρ_{AHE}-B characteristic for MNP samples annealed in various environment. All samples show nonlinearity and saturation.

I also prepared test samples with three different MNP coverage on graphene surface for about 57%, 73% and 84%, as shown by the SEM images in Figure 4.8, which give typical gap sizes for uncovered region about 120, 70 and 50 nm, respectively. Hall measurements were performed on these samples and the observed AHE in these three samples in Figure 4.8 confirms the PIFM can be obtained with low MNP coverage (close to half in area) and brings up the question that how low the MNP coverage can be for achieving PIFM for further study.

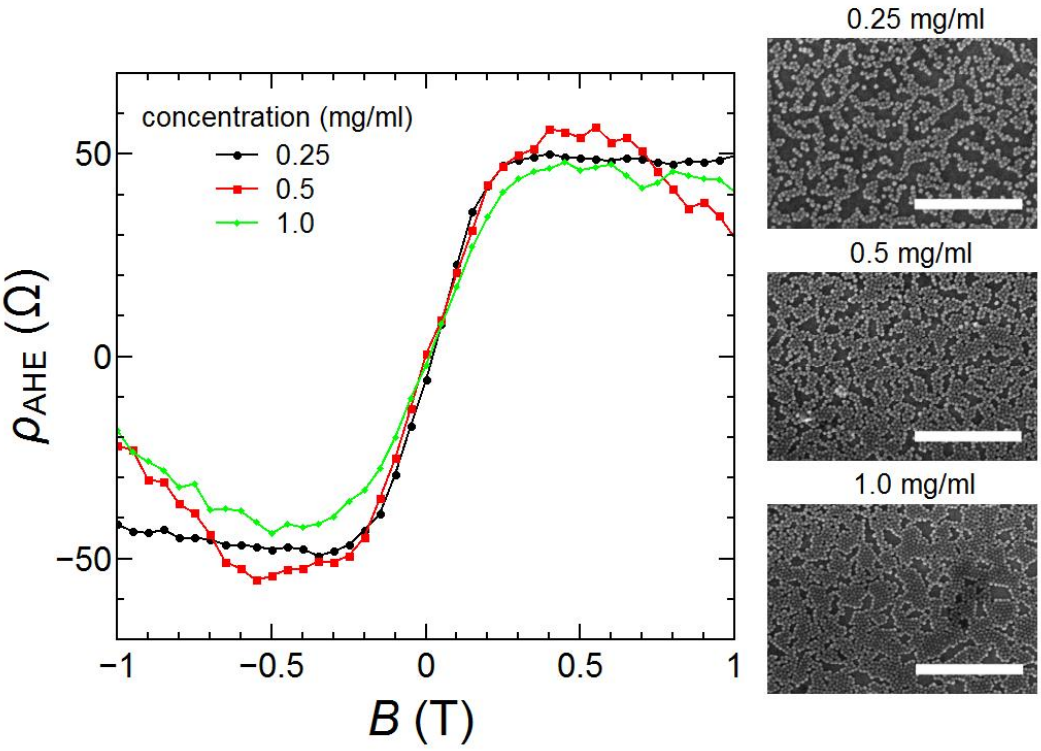

Figure 4.8 ρ_{AHE}-B characteristic for annealed samples with various MNP coverage. SEM images of the typical sample surface are shown in the bottom. PIFM is seen for all samples with different MNP coverage.

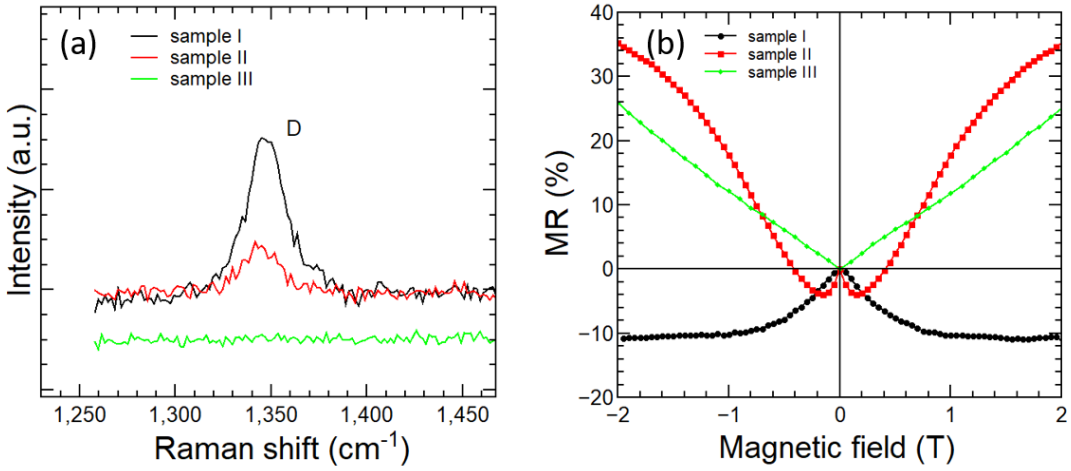

Figure 4.9 Raman spectrun and MR-*B* characteristic for three samples. Sample with high D peak shows strong weak localization. No PIFM was seen in sample III.

Graphene quality is key to achieve good electrical transport properties. Figure 4.9a shows Raman spectrum of three graphene samples with different intensity in D peak which is a signature of short-range defect in graphene. The three samples show obvious differences in MR-*B* characteristic, as depicted in Figure 4.9b. While sample I with no D peak shows weak-antilocalization feature in MR-*B* curve, sample III with high D peak shows strong weak-localization feature. Sample II with moderate D peak shows media level weak-localization characteristic. Interestingly, AHE was observed in sample I and II but not in sample III, which gives a hint that graphene quality is important to achieve PIFM and strong D peak is disadvantage. Here, we therefore propose a hypothesis that strong weak-localization in graphene can be detrimental for achieving PIFM based on these samples. A more systematic study is needed to confirm this hypothesis in future work.

4.2.5 Temperature dependence of PIFM

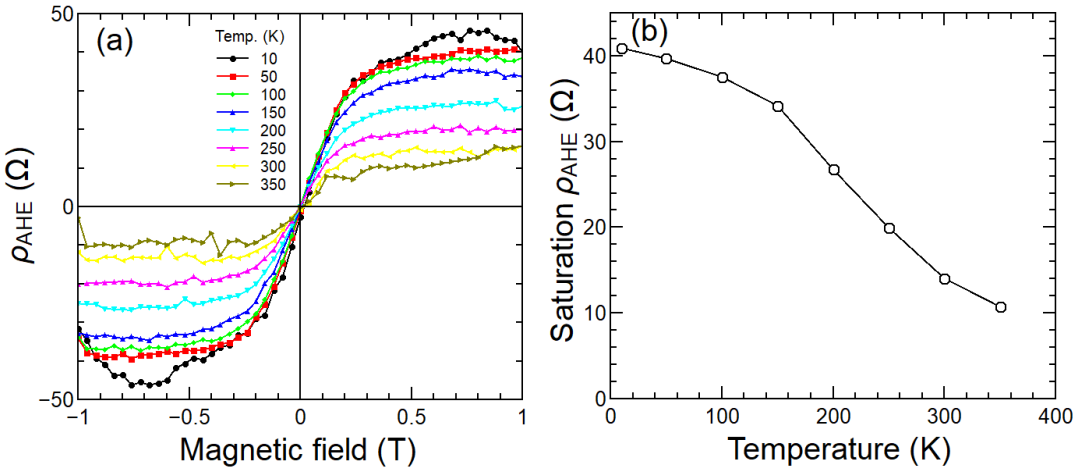

Figure 4.10 Tempeature dependence of PIFM. (a) ρ_{AHE}-B characteristics for temperature from 10 to 350 K. (b) saturation ρ_{AHE} as a function of temperearture.

Room temperature ferromagnetism is always desirable for spintronic applications. Thus, I examined the temperature dependence of ρ_{AHE}. Figure 4.10a shows the extracted ρ_{AHE}-B characteristics over the range from 10 to 350 K. The variation of saturation ρ_{AHE} with temperature is shown in Figure 4.10b and exhibits slow change with temperature below about 145 K, which corresponds closely to the blocking temperature for the MNP array observed in the magnetometry data in Figure 2.10b. Above 145 K, saturated ρ_{AHE} decreases with increasing temperature at a rate of 0.6%/K. Saturation ρ_{AHE} at 300 K is 34.3% of its value at 10 K. By extrapolating the ρ_{AHE}-T plot, the effective T_C, where ρ_{AHE} goes to zero, is about 400 K. Using the equation below from Kittel [75],

$$J = \frac{3k_B T_C}{2zS(S+1)} \quad (4.1),$$

where J is exchange energy, k_B is Boltzmann constant, T_C is Currie temperature, z is nearest neighbors and S is spin number. J is estimated to be 8.6 meV, taking is T_C = 400

K, z = 3 and S = 1, which is comparable to the exchange energy reported on graphene/EuS structure [29]. The persistence of the PIFM at temperatures far above the blocking temperature, where the MNP are superparamagnetic, is a scientifically interesting and technically useful feature of this effect.

4.2.6 Gate-tunable PIFM

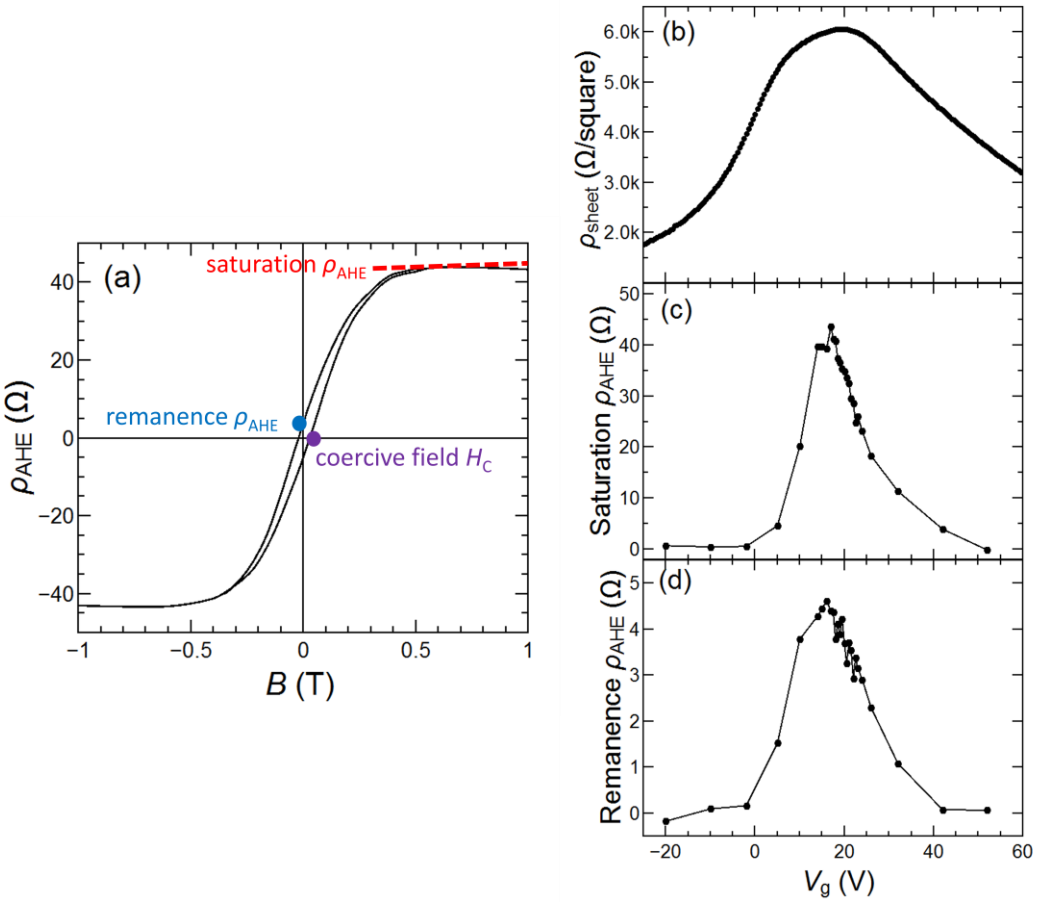

Figure 4.11 Gate bias dependence of AHE. (a) definition of saturation ρ_{AHE}, remanence ρ_{AHE} and coercive field H_c. ρ_{sheet}-V_g, saturation ρ_{AHE}-V_g, remanence ρ_{AHE}-V_g characteristics were shown in (b), (c) and (d), respectively. AHE is strong near the Dirac with FMHM about 20 V.

Gate-tunable ferromagnetism is desirable in the field of spintronics. A back-gated graphene device provides a simple structure to apply a gate bias and to investigate this possibility. In the earlier discussion, we see there is a strong gate bias dependence of saturation ρ_{AHE} in Figure 4.2. Here I plotted ρ_{sheet}-V_g, saturation ρ_{AHE}-V_g and remanence ρ_{AHE}-V_g together with more data points to examine the gate-tunalbility of PIFM, as shown in Figure 4.11. Clearly, the AHE has a strong component near the Dirac point and goes to zero far away from Dirac point. As a rough indication of how strong the AHE is, saturation ρ_{AHE}/ρ_{sheet} at Dirac point is about 0.75% which is close to half the value 1.95% from graphene/YIG stucture [26]. The full width at half maximum (FMHM) of saturation ρ_{AHE}-V_g is about 20 V. This indicates that PIFM in the MNP/graphene structure is gate-tunalable, which could be useful for electrically controled spintronic applications.

4.3 Conclusion: PIFM

In conclusion, we have demonstrated proximity induced ferromagnetism in graphene from an adjacent Fe_3O_4 self-assembled MNP array. We conclusively proved the exchange interaction at the MNP/graphene interface. We showed that PIFM in graphene persists up to room temperature and is gate tunable. The separation between nanoparticles prevents shorting of graphene channel, thereby greatly expands the choice for suitable magnetic materials. This approach allows one to work with high quality, single domain magnetic nanoparticles and to design complex nanostructures and it also provides a simple and low-cost way to achieve PIFM in graphene for large scale applications. The capability to achieve gate-tunable PIFM from such a patterned nanostructure could enable the development of novel spintronic devices and circuits.

CHAPTER 5

SPIN TORQUE OSCILLATORS USING MNP/GRAPHENE STRUCTURE

After a short introduction of STNOs, I explain the proposed MNP STNO and its advantages. Then, I describe three methods for detecting STT and STO and gave a few examples. I show some results for preliminary measurements and outline the needed improvements for future work.

5.1 Introduction of STNOs

STNOs are a novel type of nano-scale microwave oscillators that has been of great interest since Slonczewski [76] and Berger [77] predicted the STT phenomenon [78] more than 20 years ago. STNO's operation is based on STT and MR effects. The magnetization can undergo a sustained precession at a microwave frequency due to STT from a spin polarized current [79,80]. The oscillation of magnetization in GMR or TMR devices causes the oscillation of MR, and therefore at a certain input current, the output voltage and power oscillate. A typical device configuration of GMR-STO, as shown in Figure 5.1a, has two magnetic layers: a polarizing layer with fixed magnetization and a free layer with magnetization free to oscillate due to STT.

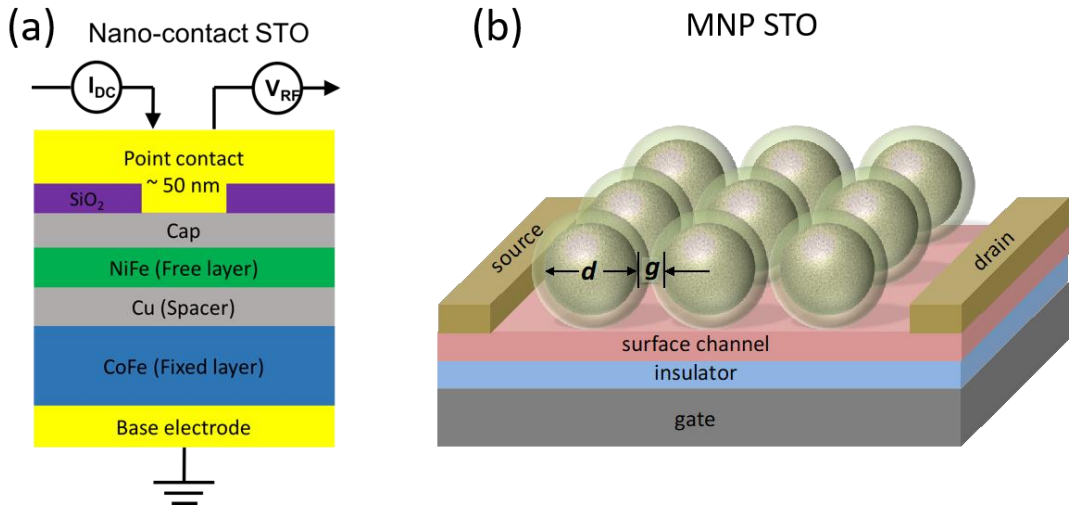

Figure 5.1 Schematic of spin torque oscillators (a) nano-contact STNO (b) MNP STNO.

The key advantages of STOs are that they can operate at high frequency approaching 100 GHz [31,81], they can be tuned by current and magnetic field over a broad frequency range of 10's of GHz [82], they are scalable down to 10's of nm (making them among the smallest microwave oscillators), and they are compatible with silicon complementary metal-oxide-semiconductor (CMOS) processes. Because of these advantages, STNOs are attractive for electrically controlled oscillator applications, such as microwave generators [33], signal-processing [83] and frequency synthesis [31]. Meanwhile, STNOs are also promising for magnetic field sensors with capabilities beyond those of the sensors as discussed above [84].

However, two serious problems of STNOs make it difficult for wide applications, that is, low output power and poor spectral purity. The size of STNOs must be small enough to keep a well-defined oscillation, which limits the output power. Phase noise of STNOs is high due to the nonlinear dynamics and electrical, magnetic fluctuations [85]. Phase locking of an array of STNOs is a promising way to increase the power and to

decrease the phase noise at the same time [35,86,87]. There are two ways to achieve phase locking, that is, injection locking STNO arrays to an external signal and mutual phase locking of coupled STNOs. Injection locking has been achieved in multiple STNOs at present [86,88]. Mutual phase locking has been demonstrated in a few STNOs [89,90]. Mutual phase locking of STNOs can occur due to several different coupling mechanisms: magnetoresistance, exchange interactions and/or dipole interactions. However, experimental demonstration of mutual phase-locked STNOs has been limited to 4 or 5 devices due to the sensitivity of STO dynamics to small structural variations and other issues [89,91]. Therefore, mutual phase locking of an array of STNOs requires precise patterning process that cannot be achieved at present with lithographic processes.

5.2 Motivation of MNP STNOs

The self-assembly technique of MNP arrays provides a new method to form STNOs. Self-assembled MNPs on a conductive surface can be driven by spin polarized current for STO, which is promising to realize phase-locked STNO arrays. Phase-locked STNO arrays can greatly improve output power and spectral purity. This chapter is focusing on a novel MNP STNO using Fe_3O_4 MNP on a graphene surface.

The proposed structure of MNP STNOs is shown in Figure 5.1b. Fe_3O_4 MNP arrays are formed on the surface channel, which is graphene in this case. The distances between MNPs are controlled by the organic shell of nanoparticles, which can be engineered as desired from 1 nanometer to about 10 nanometers [92,93]. The possible coupling mechanisms among the MNPs are i) magnetoresistance, ii) exchange interaction and iii) dipolar interaction. Each mechanism is dependent on the inter-particle distance. The control of this distance provides the freedom to modify the strength of the different

coupling interactions. Ferromagnetic source/drain contacts, such as NiFe and Co, on graphene can be used for injection of spin polarized current into the channel. STT excites the oscillation of the magnetization of MNPs. A back-gate is used to control the carrier density in the channel as an FET.

Table 5.1 Features and advantages of MNP STOs.

FEATURE	ADVANTAGE
small MNP → small *M* →	adequate STT with ultra-low I
nearly superparamagnetic →	
single crystal MNP → low loss → high Q →	robust to noise
CIP/GMR → low R → small V →	ultra-low power
self-assembled → high density →	scalable to massively parallel
tailorable MNP matl, size, spacing →	controllable *M* and coupling
lateral drive current → 2D layout →	simple fabrication
back-gate → global coupling control →	RF phase locking (pump ref)

The key advantages of the MNP STNOs are shown in Table 5.1. Small (~15nm), single domain MNPs with small coercive force only demands a small amount of STT to excite STO. This could make low current STNOs possible. Single crystal MNPs can exhibit low loss leading to high Q factor, which means robustness to noise. Since MNP STNOs use a current in-plane (CIP) GMR-like structure, the total resistance is much lower than for magnetic tunnel junction (MTJ) devices, which could make it possible for the realization of ultra-low power oscillators. The ability to self-assemble an MNP array in a large area makes it relatively easy to obtain a high density STNO array with simple process that is compatible with silicon CMOS. The tailorable properties of MNPs – including materials, size and spacing – enable the control of magnetization and coupling.

Back-gated structures can be also used for global coupling control for RF phase locking by electrically modifying the carrier density in graphene channel.

Therefore, the proposed MNP STNOs provides significant advantages for fabrication simplicity, high quality, device scalability and design flexibility, which makes MNP-STNOs promising for various applications from ultra-low power nanoscale oscillators to large array of oscillators for microwave generation with high spectral purity. Moreover, this approach could enable the development of novel information processing approaches based on arrays of locally coupled oscillators, similar to proposals for tunneling-phase logic and other nanoscale oscillator approaches [83,88].

5.3 Measurement methods

Several measurement methods have been established in previous researches for detecting STT and STO. In this section, I described three methods for studying STT in the MNP/graphene structure beyond the PIFM as discussed in Chapter 4.

5.3.1 Method (1) by ST-FMR spectrum

Ferromagnetic resonance (FMR) measurements have been widely used to study the magnetization dynamics in various systems [94–97]. STT due to the injection current can be detected by the change in resonance frequency of FMR spectrum. Figure 5.2 shows the circuit diagram for measuring V_{mix} as a function of magnetic field or frequency using ST-FMR technique. Lock-in method is employed for improving the signal-to-noise ratio of the measurements. An example of ST-FMR measurements on nanopillar STNO [97] is given in Figure 5.3. FMR was observed in V_{mix}-f spectrums and the resonance frequency

shifted with injected DC current as much as ~20%. ST-FMR is a well-established and powerful method to study STT and STOs.

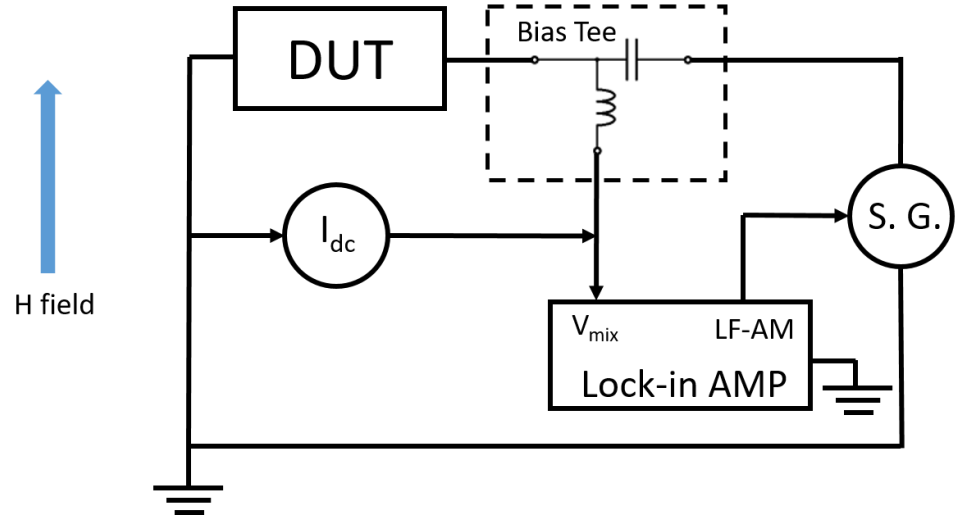

Figure 5.2 Schematic circuit diagram of the ST-FMR measurement system. AC and DC input signal are applied to the device under test (DUT) via Bias Tee. The output mixing voltage is measured by a lock-in amplifier. Magnetic field is applied in out-of-plane direction.

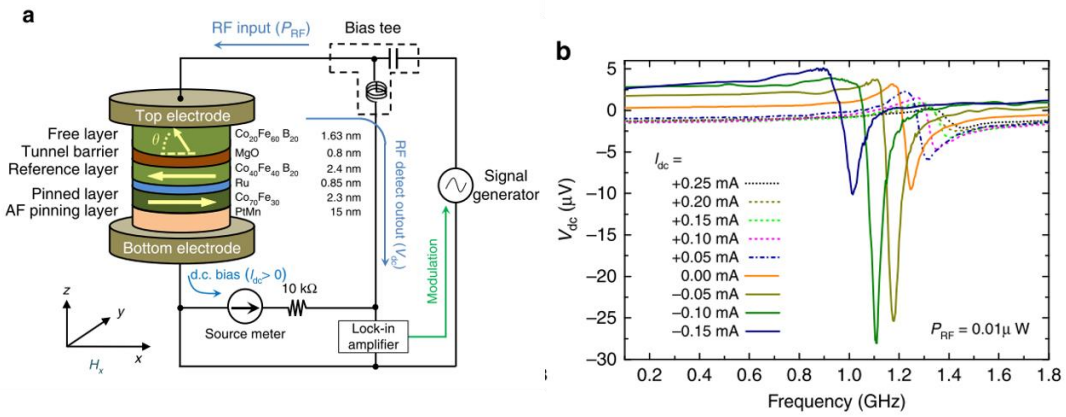

Figure 5.3 An example ST-FMR measurement on nano-pillar STNO. The resonance frequency is shifted by an applied DC current, indicating a spin transfer torque. Image adapted from Ref.[97].

5.3.2 Method (2) by *I-V* characteristics

The precession of magnetization causes the change of resistance due to MR effect, such as anisotropic magnetoresistance (AMR), GMR and TMR. The change in resistance can be detected by simple *I-V* characteristics. Current-driven magnetic excitations have been studied since the early time of STT researches in 1990s [98,99]. Figure 5.4 shows two examples of detecting current-driven magnetic excitations by monitoring the change of differential resistance. A peak in d*V*/d*I* indicates the magnetic excitation due to STT. The current level where the peak occurs is dependent on the applied magnetic field. *I-V* measurements provides a simple way to detect the STT.

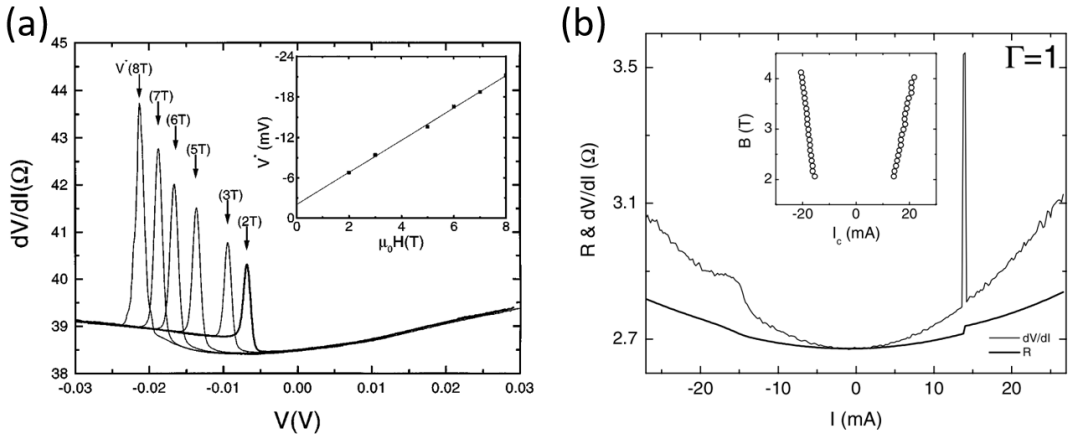

Figure 5.4 An example of detecting magnetization dynamics via *I-V* characteristics. The abrupt change in resistance is a signature of oscillation due to STT. Image adapted from Ref.[98,99].

5.3.3 Method (3) by spectrum analyzer

A direct way to detect STO is using a spectrum analyzer to measure the output signal from STNOs [33,34,87]. The oscillation frequency can be shifted by changing the

injected DC current, thereby confirming that the oscillation is due to STT. Figure 5.5 shows circuit diagram for the measurement set-up. An example of nanopillar STNO [33] studied this way by spectrum analyzer is shown in Figure 5.6. Multiple peaks correlated to different oscillation mode appear in the spectrum and the peaks shift with the injected DC current. In this method, the STT needs to be large enough to keep a steady oscillation.

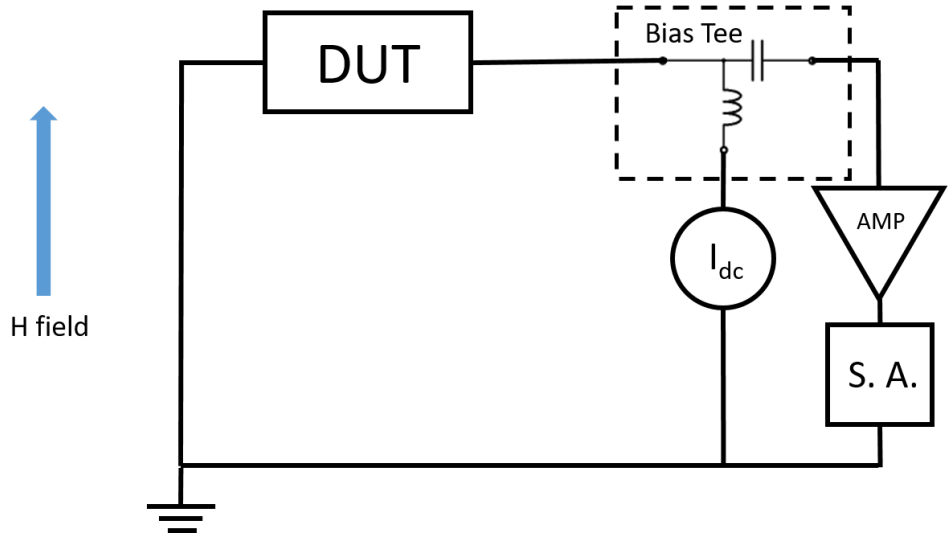

Figure 5.5 Schematic circuit diagram of the direct measurement of STO. DC current are applied to the DUT via Bias Tee. The output AC signal is measured by spectrum analyzer. Magnetic field is applied in out-of-plane direction.

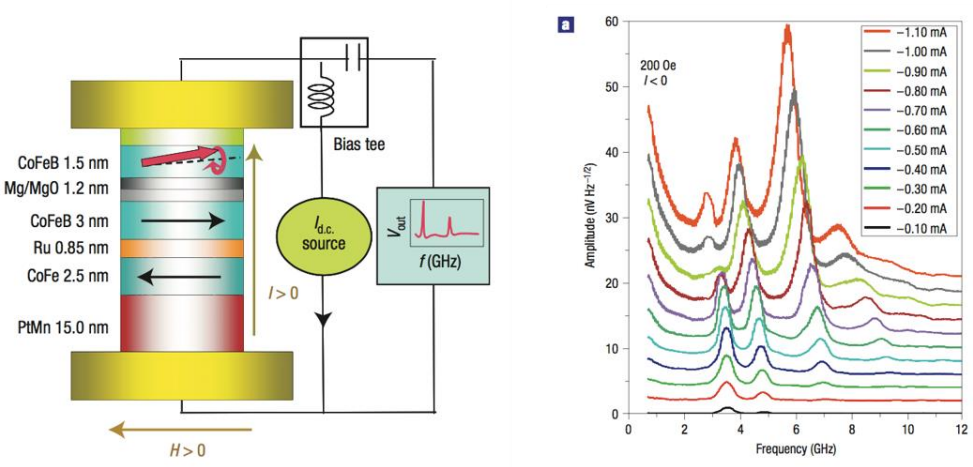

Figure 5.6 An example STO measurement by spectrum analyzer for a nanopillar STNO. The resonance frequency is shifted by an applied DC current, indicating a STT. Image adapted from Ref. [33].

5.4 Preliminary results of STO measurements and issues

All the above three methods have been adopted in the experimental study for detecting the STT in the MNP/graphene devices. First, I mainly studied devices with non-ferromagnetic contacts by using these methods. Although there is no spin injection from the contacts in this device configuration, scattering of electrons at the MNP/graphene interface might be sufficient to generate spin polarized current and thus to provide STT to MNP farther downstream. Devices with non-ferromagnetic contacts are also suitable to study FMR since no STT is required. In the section below, I present a few preliminary results using these methods.

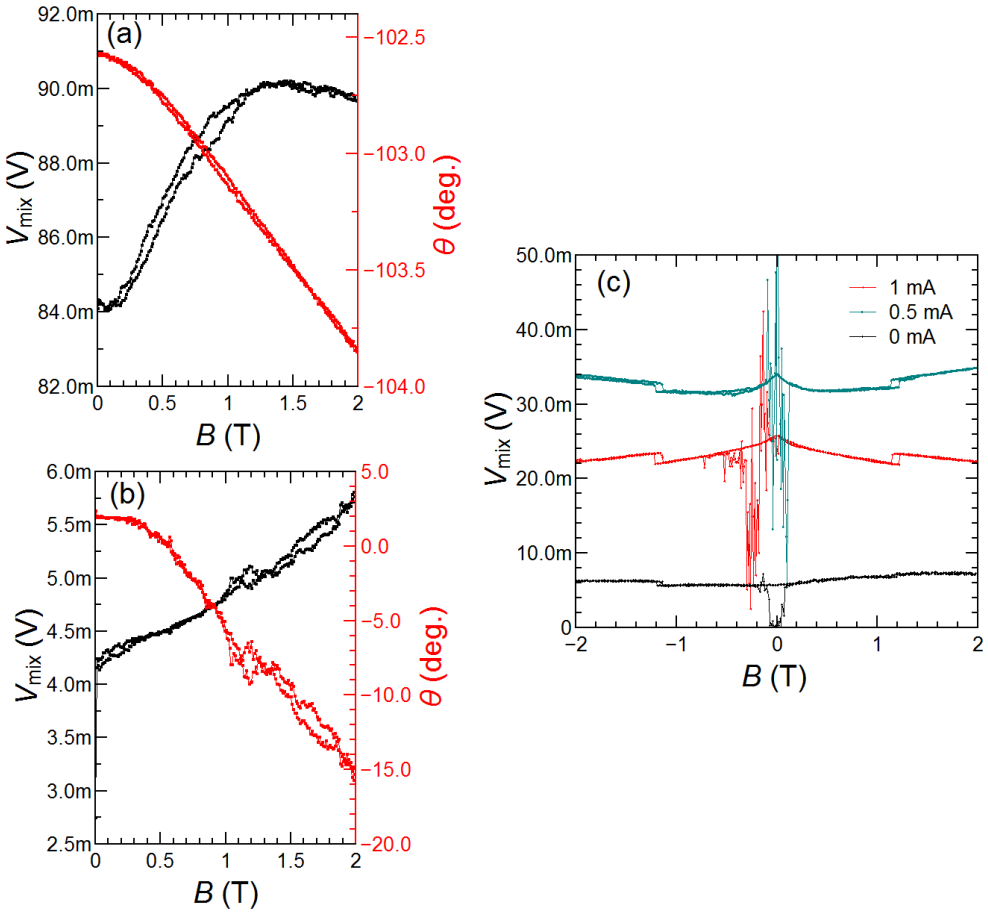

Figure 5.7 ST-FMR measurements on MNP/graphene devices. (a) and (b) V_{mix} and phase as a function of magnetic field B. (c) V_{mix}-B at various bias current.

For method (1) by ST-FMR technique, V_{mix} vs B with AC signal injection at 3 GHz are measured using the experimental set-up as illustrated in Figure 5.2. The phase changing can be monitored simultaneously. Mostly devices show a gradual changing in V_{mix} and phase due to rectification effect as shown in Figure 5.7a, which means no sign of FMR. Several devices show a step change or a sharp jump in V_{mix}, as seen in Figure 5.7b and c, respectively. This can be an indication of FMR, but more experiments are required to confirm this. For example, if STT is involved in the observed sharp jump, the B field where step in V_{mix} occurs should depend on the DC injection current, as discussed earlier.

The fact that a *B*-field dependence to the jump in the experiments was not observed does not mean that the jump is not related to FMR, but that STT may not be effective to shift the resonance *B* field in the test device. The reason for this can be attributed to the lack of spin injection since there is no ferromagnetic contact in these devices.

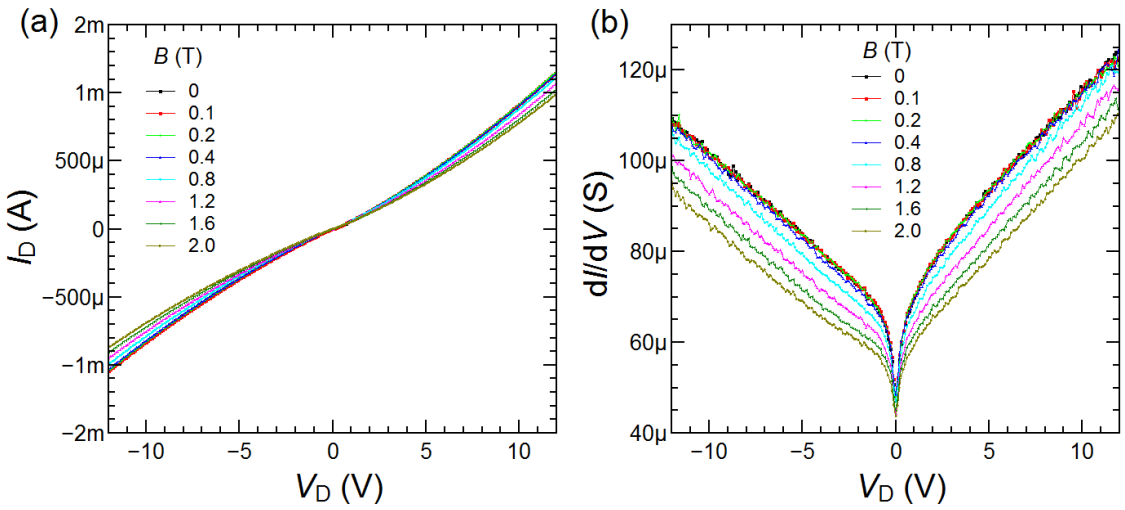

Figure 5.8 *I-V* characteristics of MNP/graphene devices with applied magnetic field applied out-of-plane.

Method (2) *I-V* characteristics and Method (3) direct measurement by spectrum analyzer have also been tried. No glitch has been seen thus far in d*I*/d*V* curves at different applied magnetic field, as shown in Figure 5.8. No peaks that were correlated with the injection current were observed by spectrum analyzer either.

Devices were also fabricated with ferromagnetic Co contacts. Although the amount of spin polarization reported for Co contacts is small [22,100], Co provides a simple fabrication scheme of providing at least some spin injection. Similar measurements have been performed using all the three methods above. However, the results on Co contact devices show similar results as the non-ferromagnetic contact devices, which indicates

the spin injection efficiency is very low as expected from previous reports [22,100], and is difficult to detect in our measurements.

To find the issues for not observing STO signals, I estimated the critical current I_C using the expression [101],

$$I_C = (\frac{2e}{\hbar})(\frac{\alpha}{\eta})\mu_0 M_s V H_{eff}, \quad (5.1)$$

where e is electron charge, $\hbar$ is reduced Planck's constant, α is Gilbert damping constant, η is spin transfer efficiency, μ_0 is permeability of vacuum, M_s is saturation magnetization and H_{eff} is effective magnetic field. Volume of all MNP is $V = W\ L\ d\ \frac{\pi}{6}$, where W is the width and L is the length of the device, d is the diameter of nanoparticles and $\frac{\pi}{6}$ is the volume filling factor for nanoparticles, as shown in Figure 5.9. For Fe_3O_4, α is ~ 0.01[102], M_s is 480 kA/m [103] and H_{eff} is taken as anisotropy field 62 kA/m at 10 K [104].

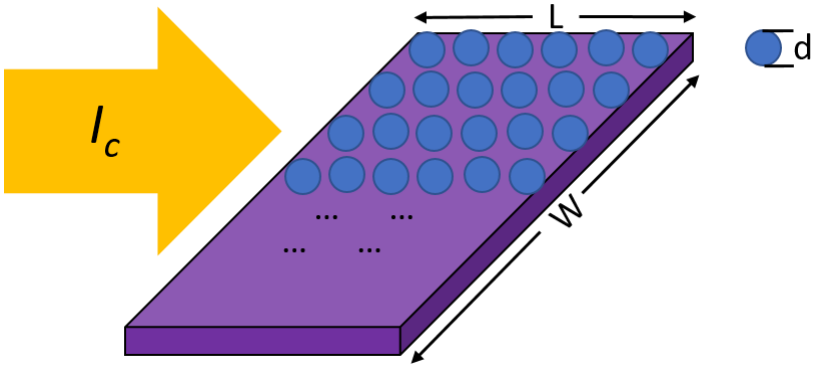

Figure 5.9 Schematic device structure of MNP/Graphene. Dimensions are labeled and I_c is the critical current for STO.

Table 5.2 Calculation results of critical current I_C for MNP array. W is 30 µm.

MNP size d = 15 nm

η	L (nm)	I_C (A)	J_C (mA/µm)
0.1	1500	4.0	133.3
0.1	150	0.4	13.33
0.1	15	0.04	1.33

MNP size d = 5 nm

η	L (nm)	I_C (A)	J_C (mA/µm)
0.35	1500	0.38	12.6
0.35	150	0.038	1.26
0.35	15	0.0013	0.13

The calculation results are shown in Table 5.2 for MNP array with two different size. For typical Co contact (η ~ 0.1), J_c is 1.33 mA/µm for short channel length which is about what graphene can provide (~ 1 mA/µm) [105]. By reducing the MNP size down to 5 nm and increasing η to 0.35 with tunneling barriers [19], J_c is 10 times lower ~0.13 mA/µm. These calculation results show graphene can provide the current required for STO by optimizing the device structures.

5.5 Limitations in the present experiments

Here I list possible explanations for not being able to detect STT and STO in the experiments thus far:

1) Insufficient spin polarization. Devices with non-ferromagnetic contacts have no spin-injection at the contacts. The possibility for spin polarization due to interface scattering with MNPs may be too small for sufficient spin polarization. Co contact on graphene has very low spin injection efficient. These issues could limit STT confirmation by all three methods.
2) Insufficient STT. The device length may be too long, and spin polarization is lost during the transport, thus there is not enough STT to drive a large MNP array.

3) Insufficient AMR. STT may be sufficient for exciting oscillation of the MNP magnetization (precession), however, the "back-coupling" of the MNP magnetization to the channel resistance may be too weak. We do not observe AMR in the experiments, at least for *B* perpendicular to the plane, thus we know that the AMR is weak. This issue would eliminate STT confirmation by Methods (2) and (3), and possibly Method (1) as well.

5.6 Suggestions for Future Improvements

Improvements for detecting STO are possible from two aspects: device and measurement. Possibilities for device improvement include:

(A) Tunnel-barrier contacts. Since Co/graphene structure has poor spin injection efficiency due to conductivity mismatch, tunneling barriers, such as Al_2O_3[21,106,107], MgO[19,23,108], TiO_2[19,23,92], SrO[109] and h-BN[100,110,111] between Co and graphene can greatly improve the spin injection efficiency, and thus provide more STT. The fabrication for advanced contacts with tunneling barriers has been shown to be effective in eliminating the conductivity mismatch problem, resulting in improvement of spin injection. However, deposition of the thin, high quality materials is difficult and has only been achieved with optimized molecular beam epitaxy. Furthermore, on the device processing side, this approach requires electron-beam lithography for minimizing surface contamination.

(B) Substrate-induced spin polarization. Ferromagnetic insulator (e.g., YIG, EuS) or topological insulator (e.g., Bi_2Te_3) substrates could be used to provide additional spin-polarization of the graphene current. This would be especially effective in the case of topological insulators, due to spin-momentum locking. Another possibility is to make use

of the spin Hall effect to provide spin polarization in the graphene, as demonstrated in previous research [94,96].

(C) Device scaling. As discussed above, short channel length devices with smaller MNP require less STT. Thereby, the critical current for exciting STO is lower.

Possiblities for improvement of STT measurement include:

(A) For Method (1) ST-FMR measurement, current modulation of lock-in technique was used at present. Magnetic field modulation, which can be generated from coils, is reported to have better signal to noise ratio [112]. Preliminary tests using magnetic field modulation have been performed. I have not observed clear signal most likely due to the modulation field is weak. The measurement could be improved by increasing the modulation field from a coil positioning close to the device under test.

(B) For Method (2) *I-V* characteristics there are several possibilities. i) Lock-in technique can be incorporated to measure differential resistance with better resolution. ii) While AMR has not been observed, we see strong effects in R_{xy} related to the transverse Hall voltage. Thus, a transverse configuration where V_{xy} is characterized might be used to overcome the lack of AMR in preliminary experiments. Preliminary tests on transverse configuration show it possible for doing measurements in this configuration with simple change of the contact layout or using wire bonding. iii) We have only explored out-of-plane magnetic field configuration in our experiments (Note: our Lakeshore system only allows out-of-plane fields). In-plane magnetic field configuration could be worth exploring since spin transfer efficiency might be improved in this configuration [30].

CHAPTER 6

SUMMARY

Graphene is a promising channel material for emerging electronic and spintronic device applications. In this dissertation, I presented my study on optimizing graphene magnetic field sensors, the first demonstration of proximity induced ferromagnetism (PIFM) in graphene from a magnetic nanoparticle (MNP) array, and a preliminary investigation of the potential of MNPs for realizing arrays of robust spin torque nano-oscillators.

The operation of graphene magnetic sensors was studied both experimentally and theoretically, especially near the charge neutrality point (CNP), where both electrons and holes exist. A two-channel model was validated by experiments and then used to predict the performance of the magnetic sensors. Linearity of the Hall characteristics and sensitivities near the CNP were carefully studied using the two-channel model. It was shown that the two-channel model provides a useful tool to study and design graphene Hall sensors. The key results show that linearity and power constraints can reduce the realizable sensitivities since the operating bias needs to be moved towards the single-carrier dominant region to meet the linearity requirement of a given application.

PIFM in graphene from an adjacent MNP array was demonstrated for the first time, where the MNP arrays were integrated with graphene using a self-assembly process. The observed anomalous Hall effect in the devices structures is a signature of PIFM. Well-designed control experiments were used to conclusively prove that the exchange interaction at the MNP/graphene interface was responsible for the observed characteristics. The PIFM in graphene persists at room temperature and is gate-tunable.

This approach greatly expands the range of suitable magnetic materials for PIFM from insulators to semiconductors, semimetals and metals, and the nanostructure opens new possibilities for spintronic devices.

The observation of PIFM in the MNP/graphene devices shows that STT from spin-polarized current in the graphene channel interacts effectively with the MNP magnetization, which opens the possibility that robust spin torque oscillations (STOs) could be realized in phase-locked MNP arrays on graphene. Three methods were used to investigate this possibility in preliminary device structures. STO has not been observed in the preliminary studies, probably because of insufficient spin-polarization in the preliminary devices. Calculation of critical current for STO shows that graphene channel should provide sufficient current in optimized device structure by reducing the device size and increasing the spin injection efficiency. The miniaturization of the device by electron beam lithography and utilization of tunnel-barrier FM contacts are promising strategies for further study.

REFERENCES

1. Dash, G. N., Pattanaik, S. R. & Behera, S. Graphene for Electron Devices: The Panorama of a Decade. *IEEE J. Electron Devices Soc.* **2**, 77–104 (2014).

2. Han, W., Kawakami, R. K., Gmitra, M. & Fabian, J. Graphene spintronics. *Nat. Nanotechnol.* **9**, 794–807 (2014).

3. Geim, A. K. & Opportunities, G. Graphene : Status and Prospects. **324**, 1530–1535 (2009).

4. Castro Neto, A. H., Guinea, F., Peres, N. M. R., Novoselov, K. S. & Geim, A. K. The electronic properties of graphene. *Rev. Mod. Phys.* **81**, 109–162 (2009).

5. Hill, E. W., Vijayaragahvan, A. & Novoselov, K. Graphene sensors. *IEEE Sens. J.* **11**, 3161–3170 (2011).

6. Schwierz, F. Graphene transistors. *Nat. Nanotechnol.* **5**, 487–496 (2010).

7. Joo, M.-K. *et al.* Large-Scale Graphene on Hexagonal-BN Hall Elements: Prediction of Sensor Performance without Magnetic Field. *ACS Nano* **10**, 8803–8811 (2016).

8. Xu, H. *et al.* Batch-fabricated high-performance graphene Hall elements. *Sci. Rep.* **3**, 1207 (2013).

9. Karpiak, B., Dankert, A. & Dash, S. P. Gate-tunable Hall sensors on large area CVD graphene protected by h-BN with 1D edge contacts. *J. Appl. Phys.* **122**, 054506 (2017).

10. Dankert, A., Karpiak, B. & Dash, S. P. Hall sensors batch-fabricated on all-CVD h-BN/graphene/h-BN heterostructures. *Sci. Rep.* **7**, 15231 (2017).

11. El-Ahmar, S. *et al.* Graphene-based magnetoresistance device utilizing strip pattern geometry. *Appl. Phys. Lett.* **110**, (2017).

12. Pisana, S., Braganca, P. M., Marinero, E. E. & Gurney, B. A. Tunable Nanoscale Graphene Magnetometers. *Nano Lett.* **10**, 341–346 (2010).

13. Lu, J. *et al.* Graphene Magnetoresistance Device in van der Pauw Geometry. *Nano Lett.* **11**, 2973–2977 (2011).

14. Xu, H. *et al.* Flicker noise and magnetic resolution of graphene hall sensors at low frequency. *Appl. Phys. Lett.* **103**, 112405 (2013).

15. Huang, L. *et al.* Graphene/Si CMOS hybrid hall integrated circuits. *Sci. Rep.* **4**, 5548 (2014).

16. Dauber, J. *et al.* Ultra-sensitive Hall sensors based on graphene encapsulated in hexagonal boron nitride. *Appl. Phys. Lett.* **106**, 193501 (2015).

17. Chen, B. *et al.* Exploration of sensitivity limit for graphene magnetic sensors. *Carbon* **94**, 585–589 (2015).

18. Huang, L. *et al.* Ultra-sensitive graphene Hall elements. *Appl. Phys. Lett.* **104**, 183106 (2014).

19. Han, W. *et al.* Tunneling Spin Injection into Single Layer Graphene. *Phys. Rev. Lett.* **105**, 167202 (2010).

20. Vera-Marun, I. J., Ranjan, V. & van Wees, B. J. Nonlinear detection of spin currents in graphene with non-magnetic electrodes. *Nat. Phys.* **8**, 313–316 (2012).

21. Tombros, N., Jozsa, C., Popinciuc, M., Jonkman, H. T. & van Wees, B. J. Electronic spin transport and spin precession in single graphene layers at room temperature. *Nature* **448**, 571–574 (2007).

22. Ohishi, M. *et al.* Spin Injection into a Graphene Thin Film at Room Temperature. *Jpn. J. Appl. Phys.* **46**, L605–L607 (2007).

23. Han, W. & Kawakami, R. K. Spin Relaxation in Single-Layer and Bilayer Graphene. *Phys. Rev. Lett.* **107**, 047207 (2011).

24. Feng, Y. P. *et al.* Prospects of spintronics based on 2D materials. *Wiley Interdiscip. Rev. Comput. Mol. Sci.* **7**, e1313 (2017).

25. Yazyev, O. V. Emergence of magnetism in graphene materials and nanostructures. *Reports Prog. Phys.* **73**, 056501 (2010).

26. Wang, Z., Tang, C., Sachs, R., Barlas, Y. & Shi, J. Proximity-Induced Ferromagnetism in Graphene Revealed by the Anomalous Hall Effect. *Phys. Rev. Lett.* **114**, 016603 (2015).

27. Leutenantsmeyer, J. C., Kaverzin, A. A., Wojtaszek, M. & van Wees, B. J. Proximity induced room temperature ferromagnetism in graphene probed with spin currents. *2D Mater.* **4**, 014001 (2016).

28. Zhang, X. *et al.* Substantially enhanced carrier mobility in graphene in proximity to ferromagnetic insulator EuS. *Appl. Phys. Express* **10**, 055103 (2017).

29. Wei, P. *et al.* Strong interfacial exchange field in the graphene/EuS heterostructure. *Nat. Mater.* **15**, 711–716 (2016).

30. Sattler, K. D. Spin-Transfer Nano-Oscillators 38.1. *Handb. nanophysics Funct. Nanomater.* 38–1 (2010). doi:10.1201/9781420075533-45

31. Bonetti, S., Muduli, P., Mancoff, F. & Åkerman, J. Spin torque oscillator frequency versus magnetic field angle: The prospect of operation beyond 65 GHz. *Appl. Phys. Lett.* **94**, 102507 (2009).

32. Mancoff, F. B., Rizzo, N. D., Engel, B. N. & Tehrani, S. Area dependence of high-frequency spin-transfer resonance in giant magnetoresistance contacts up to 300 nm diameter. *Appl. Phys. Lett.* **88**, (2006).

33. Deac, A. M. *et al.* Bias-driven large power microwave emission from MgO-based tunnel magnetoresistance devices. *Nat. Phys.* **4**, 803–809 (2008).

34. Tulapurkar, A. A. *et al.* Spin-torque diode effect in magnetic tunnel junctions. *Nature* **438**, 339–342 (2005).

35. Kaka, S. *et al.* Mutual phase-locking of microwave spin torque nano-oscillators. *Nature* **437**, 389–392 (2005).

36. Ferrari, A. C. Raman spectroscopy of graphene and graphite: Disorder, electron–phonon coupling, doping and nonadiabatic effects. *Solid State Commun.* **143**, 47–57 (2007).

37. Malard, L. M., Pimenta, M. A., Dresselhaus, G. & Dresselhaus, M. S. Raman spectroscopy in graphene. *Phys. Rep.* **473**, 51–87 (2009).

38. Ferrari, A. C. & Basko, D. M. Raman spectroscopy as a versatile tool for studying the properties of graphene. *Nat. Nanotechnol.* **8**, 235–246 (2013).

39. Fan, J. *et al.* Investigation of the influence on graphene by using electron-beam and photo-lithography. *Solid State Commun.* **151**, 1574–1578 (2011).

40. Dong, A., Chen, J., Vora, P. M., Kikkawa, J. M. & Murray, C. B. Binary nanocrystal superlattice membranes self-assembled at the liquid–air interface. *Nature* **466**, 474–477 (2010).

41. Chen, J. *et al.* Bistable Magnetoresistance Switching in Exchange-Coupled $CoFe_2O_4$–Fe_3O_4 Binary Nanocrystal Superlattices by Self-Assembly and Thermal Annealing. *ACS Nano* **7**, 1478–1486 (2013).

42. Wang, J., Wu, W., Zhao, F. & Zhao, G. Curie temperature reduction in SiO_2-coated ultrafine Fe_3O_4 nanoparticles: Quantitative agreement with a finite-size scaling law. *Appl. Phys. Lett.* **98**, 083107 (2011).

43. van der PAUW, L. J. A method of measuring specific resistivity and Hall effect of discs of arbitrary shape. *Philips Res. Rep* **13**, 1–9 (1958).

44. ASTM F76-08(2016)e1 Standard Test Methods for Measuring Resistivity and Hall Coefficient and Determining Hall Mobility in Single-Crystal Semiconductors. *ASTM International* doi:10.1520/F0076-08R16E01 (West Conshohocken, PA,

2016).

45. Song, G., Ranjbar, M. & Kiehl, R. A. Operation of graphene magnetic field sensors near the charge neutrality point. *Commun. Phys.* **2**, 65 (2019).

46. Gopinadhan, K. *et al.* Extremely large magnetoresistance in few-layer graphene/boron–nitride heterostructures. *Nat. Commun.* **6**, 8337 (2015).

47. Popovic, R. S. *Hall Effect Devices, Second Edition*. (CRC Press, 2003).

48. Bando, M. *et al.* High sensitivity and multifunctional micro-Hall sensors fabricated using InAlSb/InAsSb/InAlSb heterostructures. *J. Appl. Phys.* **105**, 07E909 (2009).

49. Das Sarma, S., Adam, S., Hwang, E. H. & Rossi, E. Electronic transport in two-dimensional graphene. *Rev. Mod. Phys.* **83**, 407–470 (2011).

50. Adam, S., Hwang, E. H., Galitski, V. M. & Das Sarma, S. A self-consistent theory for graphene transport. *Proc. Natl. Acad. Sci.* **104**, 18392–18397 (2007).

51. Martin, J. *et al.* Observation of electron–hole puddles in graphene using a scanning single-electron transistor. *Nat. Phys.* **4**, 144–148 (2008).

52. Zhang, Y., Brar, V. W., Girit, C., Zettl, A. & Crommie, M. F. Origin of spatial charge inhomogeneity in graphene. *Nat. Phys.* **5**, 722–726 (2009).

53. Hwang, E. H., Adam, S. & Das Sarma, S. Transport in chemically doped graphene in the presence of adsorbed molecules. *Phys. Rev. B* **76**, 195421 (2007).

54. Cho, S. & Fuhrer, M. S. Charge transport and inhomogeneity near the minimum conductivity point in graphene. *Phys. Rev. B* **77**, 081402 (2008).

55. Tiwari, R. P. & Stroud, D. Model for the magnetoresistance and Hall coefficient of inhomogeneous graphene. *Phys. Rev. B* **79**, 165408 (2009).

56. Knap, M., Sau, J. D., Halperin, B. I. & Demler, E. Transport in Two-Dimensional Disordered Semimetals. *Phys. Rev. Lett.* **113**, 186801 (2014).

57. Meric, I. *et al.* Current saturation in zero-bandgap, top-gated graphene field-effect transistors. *Nat. Nanotechnol.* **3**, 654–659 (2008).

58. Alekseev, P. S. *et al.* Magnetoresistance in Two-Component Systems. *Phys. Rev. Lett.* **114**, 156601 (2015).

59. Vasileva, G. Y. *et al.* Linear magnetoresistance in compensated graphene bilayer. *Phys. Rev. B* **93**, 195430 (2016).

60. Banszerus, L. *et al.* Ultrahigh-mobility graphene devices from chemical vapor deposition on reusable copper. *Sci. Adv.* **1**, e1500222 (2015).

61. Yamoah, M. A., Yang, W., Pop, E. & Goldhaber-Gordon, D. High-Velocity Saturation in Graphene Encapsulated by Hexagonal Boron Nitride. *ACS Nano* **11**, 9914–9919 (2017).

62. Bolotin, K. I., Sikes, K. J., Hone, J., Stormer, H. L. & Kim, P. Temperature-Dependent Transport in Suspended Graphene. *Phys. Rev. Lett.* **101**, 096802 (2008).

63. Lee, J., Tao, L., Hao, Y., Ruoff, R. S. & Akinwande, D. Embedded-gate graphene transistors for high-mobility detachable flexible nanoelectronics. *Appl. Phys. Lett.* **100**, 152104 (2012).

64. Srivastava, P. K., Arya, S., Kumar, S. & Ghosh, S. Relativistic nature of carriers: Origin of electron-hole conduction asymmetry in monolayer graphene. *Phys. Rev. B* **96**, 241407 (2017).

65. Huard, B., Stander, N., Sulpizio, J. A. & Goldhaber-Gordon, D. Evidence of the role of contacts on the observed electron-hole asymmetry in graphene. *Phys. Rev. B* **78**, 121402 (2008).

66. Farmer, D. B. *et al.* Chemical Doping and Electron−Hole Conduction Asymmetry in Graphene Devices. *Nano Lett.* **9**, 388–392 (2009).

67. Hannes, W.-R., Jonson, M. & Titov, M. Electron-hole asymmetry in two-terminal graphene devices. *Phys. Rev. B* **84**, 045414 (2011).

68. Han, W. *et al.* Electron-Hole Asymmetry of Spin Injection and Transport in Single-Layer Graphene. *Phys. Rev. Lett.* **102**, 137205 (2009).

69. Averyanov, D. V. *et al.* High-Temperature Magnetism in Graphene Induced by Proximity to EuO. *ACS Appl. Mater. Interfaces* **10**, 20767–20774 (2018).

70. Wu, Y.-F. *et al.* Magnetic proximity effect in graphene coupled to a $BiFeO_3$ nanoplate. *Phys. Rev. B* **95**, 195426 (2017).

71. Su, S., Barlas, Y., Li, J., Shi, J. & Lake, R. K. Effect of intervalley interaction on band topology of commensurate graphene/EuO heterostructures. *Phys. Rev. B* **95**, 075418 (2017).

72. Cheng, G. *et al.* Graphene in proximity to magnetic insulating LaMnO 3. *Appl. Phys. Lett.* **105**, 133111 (2014).

73. Swartz, A. G., Odenthal, P. M., Hao, Y., Ruoff, R. S. & Kawakami, R. K. Integration of the Ferromagnetic Insulator EuO onto Graphene. *ACS Nano* **6**, 10063–10069 (2012).

74. Nagaosa, N., Sinova, J., Onoda, S., MacDonald, a. H. & Ong, N. P. Anomalous Hall effect. *Rev. Mod. Phys.* **82**, 1539–1592 (2010).

75. Kittel, C. *Introduction to Solid State Physics*. (Wiley, 1995).

76. Slonczewski, J. C. Current-driven excitation of magnetic multilayers. *J. Magn. Magn. Mater.* **159**, L1–L7 (1996).

77. Berger, L. Emission of spin waves by a magnetic multilayer traversed by a current. *Phys. Rev. B* **54**, 9353–9358 (1996).

78. Chen, T. *et al.* Spin-Torque and Spin-Hall Nano-Oscillators. *Proc. IEEE* **104**, 1919–1945 (2016).

79. Slavin, A. & Tiberkevich, V. Nonlinear Auto-Oscillator Theory of Microwave Generation by Spin-Polarized Current. *IEEE Trans. Magn.* **45**, 1875–1918 (2009).

80. Silva, T. J. & Rippard, W. H. Developments in nano-oscillators based upon spin-transfer point-contact devices. *J. Magn. Magn. Mater.* **320**, 1260–1271 (2008).

81. Villard, P. *et al.* A GHz Spintronic-Based RF Oscillator. *IEEE J. Solid-State Circuits* **45**, 214–223 (2010).

82. Rippard, W., Pufall, M., Kaka, S., Silva, T. & Russek, S. Current-driven microwave dynamics in magnetic point contacts as a function of applied field angle. *Phys. Rev. B* **70**, 100406 (2004).

83. Kiehl, R. A. Information Processing by Nonlinear Phase Dynamics in Locally Connected Arrays. http://arxiv.org/abs/1603.06665 (2016).

84. Braganca, P. M. *et al.* Nanoscale magnetic field detection using a spin torque oscillator. *Nanotechnology* **21**, 235202 (2010).

85. Kim, J.-V., Tiberkevich, V. & Slavin, A. N. Generation Linewidth of an Auto-Oscillator with a Nonlinear Frequency Shift: Spin-Torque Nano-Oscillator. *Phys. Rev. Lett.* **100**, 017207 (2008).

86. Rippard, W. H. *et al.* Injection Locking and Phase Control of Spin Transfer Nano-oscillators. *Phys. Rev. Lett.* **95**, 067203 (2005).

87. Mancoff, F. B., Rizzo, N. D., Engel, B. N. & Tehrani, S. Phase-locking in double-point-contact spin-transfer devices. *Nature* **437**, 393–395 (2005).

88. Fan, D., Maji, S., Yogendra, K., Sharad, M. & Roy, K. Injection-Locked Spin Hall-Induced Coupled-Oscillators for Energy Efficient Associative Computing. *IEEE Trans. Nanotechnol.* **14**, 1083–1093 (2015).

89. Sani, S. *et al.* Mutually synchronized bottom-up multi-nanocontact spin–torque oscillators. *Nat. Commun.* **4**, 2731 (2013).

90. Houshang, A. *et al.* Spin-wave-beam driven synchronization of nanocontact spin-

torque oscillators. *Nat. Nanotechnol.* **11**, 280–286 (2016).

91. Csaba, G. & Porod, W. Computational study of spin-torque oscillator interactions for non-Boolean computing applications. *IEEE Trans. Magn.* **49**, 4447–4451 (2013).

92. Ye, X. *et al.* Structural diversity in binary superlattices self-assembled from polymer-grafted nanocrystals. *Nat. Commun.* **6**, 10052 (2015).

93. Park, J. *et al.* Ultra-large-scale syntheses of monodisperse nanocrystals. *Nat. Mater.* **3**, 891–895 (2004).

94. Liu, L., Moriyama, T., Ralph, D. C. & Buhrman, R. A. Spin-Torque Ferromagnetic Resonance Induced by the Spin Hall Effect. *Phys. Rev. Lett.* **106**, 036601 (2011).

95. Harder, M., Gui, Y. & Hu, C.-M. Electrical detection of magnetization dynamics via spin rectification effects. *Phys. Rep.* **661**, 1–59 (2016).

96. Mellnik, A. R. *et al.* Spin-transfer torque generated by a topological insulator. *Nature* **511**, 449–451 (2014).

97. Fang, B. *et al.* Giant spin-torque diode sensitivity in the absence of bias magnetic field. *Nat. Commun.* **7**, 11259 (2016).

98. Tsoi, M., Sun, J. Z. & Parkin, S. S. P. Current-driven excitations in symmetric magnetic nanopillars. *Phys. Rev. Lett.* **93**, 036602–1 (2004).

99. Tsoi, M. *et al.* Excitation of a magnetic multilayer by an electric current. *Phys. Rev. Lett.* **80**, 4281–4284 (1998).

100. Kamalakar, M. V., Dankert, A., Bergsten, J., Ive, T. & Dash, S. P. Enhanced tunnel spin injection into graphene using chemical vapor deposited hexagonal boron nitride. *Sci. Rep.* **4**, 6146 (2014).

101. Katine, J. A. & Fullerton, E. E. Device implications of spin-transfer torques. *J. Magn. Magn. Mater.* **320**, 1217–1226 (2008).

102. Serrano-Guisan, S. *et al.* Thickness dependence of the effective damping in epitaxial Fe_3O_4/MgO thin films. *J. Appl. Phys.* **109**, 013907 (2011).

103. Coey, J. M. D. *Magnetism and Magnetic Materials*. (Cambridge University Press, 2010). doi:10.1017/CBO9780511845000

104. A., M. & C., K. Low Curie-transition temperature and superparamagnetic nature of Fe_3O_4 nanoparticles prepared by colloidal nanocrystal synthesis. *Mater. Chem. Phys.* **192**, 235–243 (2017).

105. Meric, I. *et al.* Channel length scaling in graphene field-effect transistors studied

with pulsed current-voltage measurements. *Nano Lett.* **11**, 1093–1097 (2011).

106. Popinciuc, M. *et al.* Electronic spin transport in graphene field-effect transistors. *Phys. Rev. B* **80**, 214427 (2009).

107. Józsa, C., Popinciuc, M., Tombros, N., Jonkman, H. T. & van Wees, B. J. Controlling the efficiency of spin injection into graphene by carrier drift. *Phys. Rev. B* **79**, 081402 (2009).

108. Pi, K. *et al.* Manipulation of Spin Transport in Graphene by Surface Chemical Doping. *Phys. Rev. Lett.* **104**, 187201 (2010).

109. Singh, S. *et al.* Strontium Oxide Tunnel Barriers for High Quality Spin Transport and Large Spin Accumulation in Graphene. *Nano Lett.* **17**, 7578–7585 (2017).

110. Gurram, M., Omar, S. & Wees, B. J. van. Bias induced up to 100% spin-injection and detection polarizations in ferromagnet/bilayer-hBN/graphene/hBN heterostructures. *Nat. Commun.* **8**, 248 (2017).

111. Wu, Q. *et al.* Efficient Spin Injection into Graphene through a Tunnel Barrier: Overcoming the Spin-Conductance Mismatch. *Phys. Rev. Appl.* **2**, 044008 (2014).

112. Gonçalves, A. M. *et al.* Spin torque ferromagnetic resonance with magnetic field modulation. *Appl. Phys. Lett.* **103**, 172406 (2013).

APPENDIX A

LIST OF ACRONYMS

2DEG	two-dimensional electron gas
AFM	atomic force microscope
AHE	anomalous Hall effect
AMR	anisotropic magnetoresistance
BNSL	binary nanocrystal supperlattice
C-AFM	conductive atomic force microscope
CIP	current in-plane
CMOS	complementary metal-oxide-semiconductor
CNP	charge neutrality point
CVD	chemical vapor deposition
DUT	device under test
EG	ethylene glycol
FET	field-effect transistor
FMI	ferromagnetic insulator
FMR	ferromagnetic resonance
FTIR	Fourier-transform infrared spectroscopy
FWHM	full-width at half-maximum
GMR	giant magnetoresistance
h-BN	hexagonal Boron Nitride
IPA	isopropyl alcohol
MNP	magnetic nanoparticle
MR	magnetoresistance
MTJ	magnetic tunnel junction

OHE	ordinary Hall effect
PIFM	proximity induced ferromagnetism
PR	photoresist
RTA	rapid thermal annealing
SEM	scanning electron microscope
SOC	spin orbit coupling
STNO	spin torque nano-oscillator
STO	spin torque oscillation
STT	spin transfer torque
TEM	transmission electron microscopy
TMR	tunneling magnetoresistance
VSM	vibrating-sample magnetometer
YIG	yttrium iron garnet

APPENDIX B

MATLAB CODE FOR TWO-CHANNEL MODEL SIMULATIONS

B.1 S_I vs V_g simulations

```
clc;
clear all;
close all;

e=1.6*10^-19; %C
Cox=12.1*10^-9; %F
%a=0.785;
vDirac=0; %V

n0=1*10^11;
u=20000;
x=-2:0.01:2; %Magnetic field B
delta_vg=0.01;

%dimension
d1=length(x);
d2=80/delta_vg+1;

v_i=zeros(1, d2);
M_ne_i=zeros(1,d2);
M_nh_i=zeros(1,d2);

Max_alpha_i=zeros(1, d2);
M_Rxy_i=zeros(d1,d2);
M_Rxy_fit_i=zeros(d1,d2);
M_alpha_i=zeros(d1,d2);
SI_i=zeros(1, d2);

    for a=1:d2
        ue=u;
        uh=u;
        vg=-40+delta_vg*(a-1);
        v_i(a)=vg;

        n=-Cox/e*(vg-vDirac);
        ne=1/2*(-n+sqrt(n0.^2+n.^2));
        M_ne_i(a)=ne;
        nh=1/2*(n+sqrt(n0.^2+n.^2));
        M_nh_i(a)=nh;

            Rxy=(-((1.6.*ne.*ue.^2.*x)/10^23./(1                          +
(ue.^2.*x.^2)/100000000))+(1.6.*nh.*uh.^2.*x)/10^23./(1                   +
(uh.^2.*x.^2)/100000000))./(((1.6.*ne.*ue)/10^19./(1                      +
(ue.^2.*x.^2)/100000000)+           (1.6.*nh.*uh)/10^19./(1               +
(uh.^2.*x.^2)/100000000)).^2      +(-((1.6.*ne.*ue^2.*x)/10^23./(1        +
(ue.^2.*x.^2)/100000000))+(1.6.*nh.*uh.^2.*x)/10^23./(1                   +
(uh.^2.*x.^2)/100000000)).^2);
            P = polyfit(x,Rxy,1);
            Rxy_fit = P(1)*x+P(2);
            alpha=abs(Rxy./Rxy_fit-1)*100; %in percent
            alpha((d1+1)/2)=0;
            Max_alpha_i(a)=max(alpha);
```

```
         SI_i(a)=abs(P(1));

        M_Rxy_i(:,a)=Rxy';
        M_Rxy_fit_i(:,a)=Rxy_fit';
        M_alpha_i(:,a)=alpha';

end

M_ne_nh=[v_i' M_ne_i' M_nh_i'];
M_Max_alpha=[v_i' Max_alpha_i'];
M_SI=[v_i' SI_i'];

M_Rxy=[x' M_Rxy_i];
M_Rxy_fit=[x' M_Rxy_fit_i];
M_alpha=[x' M_alpha_i];

M_all=[v_i' SI_i' Max_alpha_i'];


c=(d2+1)/2;
%c=340;
figure('Name','Max_alpha vs Vg');
scatter(v_i,Max_alpha_i)
xlim([-20 20])
figure('Name','SI vs Vg');
scatter(v_i,SI_i)
xlim([-20 20])
figure('Name','ne nh vs Vg');
scatter(v_i,M_ne_i)
hold on;
scatter(v_i,M_nh_i)
hold off;

figure('Name','alpha vs B');
scatter(x,M_alpha(:,c))
figure('Name','Rxy vs B');
scatter(x,M_Rxy(:,c))
hold on;
scatter(x,M_Rxy_fit(:,c),'.')
```

B.2 MR vs V_g simulaitons

```
clc;
clear all;
close all;

e=1.6*10^-19; %C
Cox=12.1*10^-9; %F
%a=0.785;
u=5000;
vDirac=0; %V
x=-2:0.01:2; %Magnetic field B
delta_vg=0.01;

%dimension
d1=length(x);
d2=80/delta_vg+1;

v_i=zeros(1, d2);
M_ne_i=zeros(1,d2);
M_nh_i=zeros(1,d2);

MR_i=zeros(1,d2);
M_Rxx_i=zeros(d1,d2);

    for a=1:d2
        n0=1*10^11;
        ue=u;
        uh=u;
        vg=-40+delta_vg*(a-1);
        v_i(a)=vg;

        n=-Cox/e*(vg-vDirac);
        ne=1/2*(-n+sqrt(n0.^2+n.^2));
        M_ne_i(a)=ne;
        nh=1/2*(n+sqrt(n0.^2+n.^2));
        M_nh_i(a)=nh;

        % Rxy=ue./uh.^2.*(ne./nh).*x.^2;
        Rxx=(((1.6.*ne.*ue)/10^19./(1                                    +
(ue.^2.*x.^2)/100000000))+(1.6.*nh.*uh)/10^19./(1                        +
(uh.^2.*x.^2)/100000000))./(((1.6.*ne.*ue)/10^19./(1                     +
(ue.^2.*x.^2)/100000000)+           (1.6.*nh.*uh)/10^19./(1              +
(uh.^2.*x.^2)/100000000)).^2      +(-((1.6.*ne.*ue^2.*x)/10^23./(1       +
(ue.^2.*x.^2)/100000000))+(1.6.*nh.*uh.^2.*x)/10^23./(1                  +
(uh.^2.*x.^2)/100000000)).^2);
            MR_i(a) = (Rxx(d1)/Rxx((d1+1)/2)-1)*100; % in percent

            M_Rxx_i(:,a)=Rxx';
    end

    M_ne_nh=[v_i' M_ne_i' M_nh_i'];
    M_MR=[v_i' MR_i'];
```

```
M_Rxx=[x' M_Rxx_i];

c=(d2+1)/2;
figure('Name','MR vs Vg');
scatter(v_i,MR_i)
figure('Name','Rxx vs B');
scatter(x,M_Rxx(:,c))
```

B.3 Realizable sensitivities vs mobility simulations

```
clc;
clear all;
close all;

e=1.6*10^-19; %C
Cox=12.1*10^-9; %F
%a=0.785;
vDirac=0; %V
n0=1*10^11; %minimum carrier density
x=-2:0.01:2; %Magnetic field B
delta_vg=0.01;
%dimension
d1=length(x);
d2=80/delta_vg+1;

v_i=zeros(1, d2);
M_ne_i=zeros(1,d2);
M_nh_i=zeros(1,d2);

Max_alpha_i=zeros(1, d2);
M_Rxy_i=zeros(d1,d2);
M_Rxy_fit_i=zeros(d1,d2);
M_alpha_i=zeros(d1,d2);
SI_i=zeros(1, d2);
rho_s_i=zeros(1,d2);
SA_i=zeros(1,d2); % SA at 1mW power

percent=1; %alpha percentage limitation
d3=100;
u_i=logspace(2,6,d3);
M_SI_vs_u_i=zeros(1,d3);
M_SA_vs_u_i=zeros(1,d3);
M_Max_alpha_vs_u_i=zeros(1,d3);
M_I=zeros(1,d3);
M_vg_I=zeros(1,d3);
M_rho_s_I=zeros(1,d3);

power=10^-3; % power supply in Walt

tic
for c=1:d3
    u=u_i(c);
    for a=1:d2
        ue=u;
        uh=u;
        vg=-40+delta_vg*(a-1);
        v_i(a)=vg;

        n=-Cox/e*(vg-vDirac);
        ne=1/2*(-n+sqrt(n0.^2+n.^2));
        M_ne_i(a)=ne;
        nh=1/2*(n+sqrt(n0.^2+n.^2));
```

```
        M_nh_i(a)=nh;

        Rxx=(((1.6.*ne.*ue)/10^19./(1                                    +
(ue.^2.*x.^2)/100000000))+(1.6.*nh.*uh)/10^19./(1                        +
(uh.^2.*x.^2)/100000000)./(((1.6.*ne.*ue)/10^19./(1                      +
(ue.^2.*x.^2)/100000000)+            (1.6.*nh.*uh)/10^19./(1             +
(uh.^2.*x.^2)/100000000).^2      +(-((1.6.*ne.*ue^2.*x)/10^23./(1        +
(ue.^2.*x.^2)/100000000))+(1.6.*nh.*uh.^2.*x)/10^23./(1                  +
(uh.^2.*x.^2)/100000000)).^2);
        rho_s_i(a)=max(Rxx);

        Rxy=(-((1.6.*ne.*ue.^2.*x)/10^23./(1                             +
(ue.^2.*x.^2)/100000000))+(1.6.*nh.*uh.^2.*x)/10^23./(1                  +
(uh.^2.*x.^2)/100000000)./(((1.6.*ne.*ue)/10^19./(1                      +
(ue.^2.*x.^2)/100000000)+            (1.6.*nh.*uh)/10^19./(1             +
(uh.^2.*x.^2)/100000000).^2      +(-((1.6.*ne.*ue^2.*x)/10^23./(1        +
(ue.^2.*x.^2)/100000000))+(1.6.*nh.*uh.^2.*x)/10^23./(1                  +
(uh.^2.*x.^2)/100000000)).^2);
             P = polyfit(x,Rxy,1);
             Rxy_fit = P(1)*x+P(2);
             alpha=abs(Rxy./Rxy_fit-1)*100; %in percent
             alpha((d1+1)/2)=0;
             Max_alpha_i(a)=max(alpha); %alpha limitation=10%, get Vg

             SI_i(a)=abs(P(1)); % get SI at that Vg

             SA_i(a)=SI_i(a)*(power/rho_s_i(a))^0.5; % SA at 1mW power

            M_Rxy_i(:,a)=Rxy';
            M_Rxy_fit_i(:,a)=Rxy_fit';
            M_alpha_i(:,a)=alpha';

    end

    for b=(d2+1)/2:d2-1
        if   Max_alpha_i(b)>percent   &&   Max_alpha_i(b+1)<percent   &&
SA_i(b)>SA_i(b+1)

            M_SI_vs_u_i(c)=SI_i(b+1);
            M_SA_vs_u_i(c)=SA_i(b+1);
            M_Max_alpha_vs_u_i(c)=Max_alpha_i(b+1);
            M_I(c)=b+1;
            M_vg_I(c)=v_i(b+1);
            M_rho_s_I(c)=rho_s_i(b+1);
            break

        elseif b>d2-1.5

            [M,I]=max(SA_i);
            M_SA_vs_u_i(c)=M;
            M_SI_vs_u_i(c)=SI_i(I);
            M_Max_alpha_vs_u_i(c)=Max_alpha_i(I);
            M_I(c)=I;
            M_vg_I(c)=v_i(I);
            M_rho_s_I(c)=rho_s_i(I);
```

```
            %disp('All values are below the limit.')
        end
    end
end
    toc

    M_ne_nh=[v_i' M_ne_i' M_nh_i'];
    M_Max_alpha=[v_i' Max_alpha_i'];
    M_SI=[v_i' SI_i'];

    M_Rxy=[x' M_Rxy_i];
    M_Rxy_fit=[x' M_Rxy_fit_i];
    M_alpha=[x' M_alpha_i];

    %M_SA_I=M_SI_vs_u_i.*(power./M_rho_s_I).^0.5; % SA at 1mW power

    M_SI_alpha_I_vg_vs_u=[u_i'  M_SI_vs_u_i'  M_Max_alpha_vs_u_i'  M_I'
M_vg_I' M_rho_s_I' M_SA_vs_u_i'];

    m=(d2+1)/2;
    %c=340;
    figure('Name','Max_alpha vs Vg');
    scatter(v_i,Max_alpha_i)
    figure('Name','SI vs Vg');
    scatter(v_i,SI_i)
    figure('Name','SA vs Vg');
    scatter(v_i,SA_i)
    figure('Name','alpha vs B');
    scatter(x,M_alpha(:,m))
    figure('Name','Rxy vs B');
    scatter(x,M_Rxy(:,m))
    hold on;
    scatter(x,M_Rxy_fit(:,m),'.')

    figure('Name', 'Vg vs u');
    scatter(u_i,M_vg_I)
    set(gca, 'XScale', 'log')

    figure('Name', 'rho_s vs u');
    scatter(u_i,M_rho_s_I)
    set(gca, 'XScale', 'log')

    figure('Name', 'SA vs u');
    scatter(u_i,M_SA_vs_u_i)
    set(gca, 'XScale', 'log')

    figure('Name', 'SI vs u');
    scatter(u_i,M_SI_vs_u_i)
    set(gca, 'XScale', 'log')

    figure('Name', 'Max_alpha vs u');
    scatter(u_i,M_Max_alpha_vs_u_i)
    set(gca, 'XScale', 'log')
```